Accepted Manuscript

Dredging and canal gate technologies in Portus, the ancient harbour of Rome, reconstructed from event stratigraphy and multi-proxy sediment analysis

A. Lisé-Pronovost, F. Salomon, J.-P. Goiran, G. St-Onge, A.I.R. Herries, J.-C. Montero-Serrano, D. Heslop, A.P. Roberts, V. Levchenko, A. Zawadzki, H. Heijnis

PII: S1040-6182(17)31397-6

DOI: 10.1016/j.quaint.2018.05.018

Reference: JQI 7428

To appear in: *Quaternary International*

Received Date: 2 November 2017

Revised Date: 27 April 2018

Accepted Date: 11 May 2018

Dredging and Canal Gate Technologies in Portus, the Ancient Harbour of Rome, Reconstructed from Event Stratigraphy and Multi-Proxy Sediment Analysis

Lisé-Pronovost, A.[1], Salomon, F.[2, 3], Goiran, J.-P.[4], St-Onge, G.[5], Herries, A, I. R..[1], Montero-Serrano, J.-C.[5], Heslop, D.[6], Roberts, A. P.[6], Levchenko, V.[7], Zawadzki, A. [7], Heijnis, H.[7]

[1]The Australian Archaeomagnetism Laboratory, Palaeoscience Labs, Department of Archaeology and History, La Trobe University, Melbourne Campus, Bundoora, 3086, VIC, Australia
[2]Laboratoire Image Ville Environnement UMR 7362, Université de Strasbourg, 3 rue de l'Argonne 67083 Strasbourg cedex, France
[3]Department of Archaeology, University of Southampton, Southampton SO17 1BF, United Kingdom
[4]Centre national de la recherche scientifique, Maison de l'Orient et de la Méditerranée, Lyon 69365, France
[5]Institut des sciences de la mer de Rimouski, Canada Research Chair in Marine Geology, Université du Québec à Rimouski and GEOTOP, Rimouski G5L 2Z9, Québec, Canada
[6]Research School of Earth Sciences, Australian National University, Canberra, 2601, ACT, Australia
[7]Australian Nuclear Science and Technology Organisation (ANSTO), Lucas Heights, 2234, NSW, Australia

ABSTRACT

Ancient harbours are rich archives of human-environment interaction. However, dating harbour deposits and correlating their stratigraphy is a major challenge because of typically high sedimentation rates over short periods and possible curative dredging events. Portus, the maritime harbour of Rome at the height of the Roman Empire, was a port complex composed of basins and canals connecting the commercial harbour to Rome via the Tiber River. Sediment core CPS1 in the narrowest of these canals, Canale Traverso, is located centrally in what was the capital city's commercial hub and contains a continuous harbor depositional record with average sedimentation rates greater than 1 cm per year. Here we use piston coring, high-resolution core scanning and a multi-proxy sediment analysis including for the first time paleo- and rock-magnetism, and bulk and clay mineralogy in order to overcome the problems of dating harbour deposits and correlating their stratigraphy. The method allowed precise identification of major reworked events, including a dredged deposit and a hyperpycnal deposit, which improve the chronostratigraphy and water depth reconstruction, and sheds light on harbour technologies at the height of the Roman Empire. A debris layer with abundant ceramic fragments and rocks marks the decommissioning of Canale Traverso and provides a new chronostratigraphic marker at Portus. Multi-proxy riverine input signatures point to the possible use of canal gate technology for water flow management.

1. INTRODUCTION

Ancient harbour deposits around the Mediterranean Sea have high accumulation rates of up to one to four centimeters per year (Goiran and Morhange, 2001; Marriner and Morhange, 2006; 2007; Morhange and Marriner, 2010; Goiran et al., 2010; Salomon et al., 2012), which is orders of magnitude higher than in most natural environments such as lakes and oceans (Sadler, 1981). As such, ancient harbour sediment archives can potentially provide high-resolution sedimentary records. With time resolution comparable to varved lake sediment and ice core palaeoclimate records, ancient harbour archives also have the advantage of abundant historical reports. The high time resolution of ancient harbour archives is of interest across disciplines for documenting human-environment interaction, palaeoclimate and history, as well as geomagnetic field change. Such records could, for example, allow further investigation of hypothesised and debated links between climate stability and Roman Empire expansion and contraction (e.g., Büntgen et al., 2011; McCormick et al., 2012; Mensing et al., 2015).

Dating is a major challenge that impedes most interpretations of ancient harbour archives. It is challenging because of the large uncertainty of radiocarbon dating and calibration relative to the short time periods covered by ancient deposits, which typically do not exceed several hundred years (e.g., Goiran and Morhange, 2001; Salomon et al., 2012). Dating also depends on the available artefacts, if any, found within the stratigraphy, such as ceramic fragments that can be associated with a specific period. Most importantly, possible dredging of ancient harbour infrastructure significantly complicates attempts to build precise chronologies (Salomon et al., 2016). Historical reports and geoarchaeological evidence indicate that mechanical mud removal was performed to maintain sufficient draught for boats to navigate waterways since the 4th century BC, and more extensively during the Roman Empire (Morhange and Marriner, 2010). Dredging boats unearthed in Marseille constitute direct archaeological evidence for that technology (Pomey, 1995). Further stratigraphic evidence also exists such as a cut-and-fill talus exposed during excavation in

Marseilles (Morhange et al., 2003), and wedged scars in volcanic tufa bedrock in the ancient harbour of Naples (Morhange and Marriner, 2010). In sediment cores, however, dredging is at best tentatively identified from radiocarbon date inversions and chronological hiatuses (e.g., Marriner and Morhange, 2006; Marriner et al., 2006; Salomon et al., 2012; Delile et al., 2014; Goiran et al., 2014; Salomon et al., 2016; Stock et al., 2016). Extreme storm, tsunami, and flood events can also cause chronological hiatuses and 'instantaneous' deposition (St-Onge et al., 2004; Goiran et al, 2014; Vött et al, 2014; Hadler et al, 2015; Röbke and Vött 2017).

Canal gates represent another technology that may have affected sedimentation, but for which evidence is elusive. Historical reports indicate that canal gates may have been used for flood control, navigation or protection (Plinius (nat. hist. III 9,53); Bockius, 2014), yet direct physical evidence is limited to rocky ancient Mediterranean harbours, where rock walls have man-made cuttings (Allen, 1853; McCann, 1979; Erol and Pirazzoli, 1992). Without precise identification of dredging events, extreme weather events, canal gate use, and associated chronological hiatuses and/or reworked deposits within a sedimentary sequence, a precise age-depth model cannot be obtained. Precise identification of event deposits in lake and marine sediment archives is commonly achieved using piston coring to recover the most undisturbed stratigraphy, and high-resolution sediment analysis such as core scanning and magnetic properties (e.g., Duchesne et al., 2006; Storen et al., 2010; Gilli et al., 2013). There are no universal criteria to identify what caused event deposits, and consideration of the local setting and a multi-proxy approach are important. Expected sedimentological evidence for dredging includes sharp contacts, sedimentary discontinuities, and age hiatuses from removal of dredged sediment, and possibly disturbed stratigraphy and mixing of sediment layers from shoveling. In contrast, hydrodynamic high-energy storm, tsunami, flood, and canal gate control events would likely produce graded beds from changes in flow intensity and sediment transport capacity. Event deposits must be taken into account to build robust age-depth models.

Portus, the ancient harbour of Rome, is one of the best-studied ancient harbour sites (Keay et al., 2005; Keay and Paroli, 2011). The Emperor Claudius initiated Portus' construction in AD 42 near the Tiber River mouth on the Tyrrhenian Sea, with a second phase of development under the Emperor Trajan (AD 112-117) (Keay et al., 2005), which included construction of the emblematic hexagonal basin that is visible today (Fig. 1). Portus was a large harbour complex that served as the commercial hub and store for Rome at the height of the Roman Empire, receiving goods from all around the Mediterranean Sea. Today, remains of Portus are landlocked three kilometers from the coastline, with part of the port complex lying under the Leonardo da Vinci-Fiumicino International Airport. With exceptionally high sedimentation rates in its basins and canals (Giraudi et al., 2009; Goiran et al., 2010; Salomon et al., 2012; 2014, Delile et al., 2014), the sedimentary archive of Portus has the potential to provide high-resolution geoarchaeological, palaeoclimatic and paleomagnetic records. No previous study has provided precise chronologies because of: 1) the disturbed stratigraphy of cores that were drilled using rotating core barrels and extraction of sediment into plastic trays; 2) possibly unidentified hiatuses and\or event deposits; and 3) large radiocarbon dating and calibration uncertainties relative to the short period covered by the harbour deposit. As a result, age-depth models from Portus are mostly vertical with several meters of mud having the same age, and the stratigraphy of cores is difficult to correlate to each other. At Portus, sedimentary radiocarbon date inversions provide hints of dredging (Delile et al., 2014; Salomon et al., 2012; Goiran et al., 2010) and dredging in Portus basins is depicted in an epigraph at ca AD 400 (Coccia, 1993; Giraudi et al., 2009). Flood gates or canal locks were also hypothesised on the canals of Portus, including the Canale Traverso (Testaguzza, 1970), the Fossa Traiana, and the Canale Romano (Salomon et al., 2014); however, there has been no conclusive evidence for these technologies. Portus was clearly influenced by fluvial input however, no flood layer has been identified (Salomon et al., 2012; 2014). Flood and/or storm/tsunami deposits have been reported in the harbour of Ostia, also located on the Tiber delta, in the centuries preceding the construction of Portus (Goiran et al, 2014; Hadler et al, 2015; Marriner et al, 2017). Here we apply methods commonly used in marine geology, including piston coring, high-resolution core scanning, and multi-proxy sediment analyses (grain size, paleo- and rock-magnetism, and bulk and clay mineralogy), together with radiocarbon dating and Bayesian age modelling to precisely identify event deposits and to better constrain the Portus chronostratigraphy, and to document Roman harbour technologies.

2. MATERIAL AND METHODS

2.1 Field Work

Coring operations were completed in September 2011 using a stationary hydraulic piston system operated by the *Centre d'Étude Techniques de l'Équipement* (CETE) *Méditerranée*. This method allows recovery of relatively undisturbed and continuous sediment sequences with core sections preserved in polyvinyl chloride (PVC) tube liners. The cores were sealed and shipped to the *Institut des sciences de la mer de Rimouski* (ISMER) of the *Université du Québec à Rimouski* (UQAR) for analysis. Based on the high sediment accumulation rates (Salomon et al., 2012) and the results of a pilot rock-magnetic study (cf. section 2.2) it was decided to core Canale Traverso. The coring site in Canale Traverso was selected near the access channel (Fig. 1B) based on the hypothesis that the hydraulic energy would dissipate and, thus, sediment would accumulate most rapidly where canal widens. Two cores, CPS1 and CPS4, were recovered from that location (Figs. 1B, D). CPS1 was selected for high-resolution multi-proxy study because of its thicker apparent harbour deposit.

2.2 Pilot Study

Samples from previous rotary drilling at Portus (Goiran et al., 2010; Salomon et al., 2012) were analysed at ISMER prior to field work to evaluate the potential for paleo- and environmental magnetism studies at Portus. Eight sediment samples were chosen from core TR-20 in the access channel and seven samples from core CT1 in Canale Traverso (see core locations in Fig. 1B). The performed analyses include temperature dependence of magnetic susceptibility (50 to 700 ºC), alternating field (AF) demagnetisation of the natural remanent magnetisation (NRM), hysteresis properties, and isothermal remanent magnetisation (IRM) acquisition (methods summarized in Lisé-

Pronovost et al., 2013). Results of the pilot study (supplementary material 1) indicate that Canale Traverso was the most promising site with a strong magnetic signal dominated by low coercivity magnetite with single domain (SD) to vortex magnetic state, and a stable NRM, which are suitable for paleomagnetic recording (Tauxe, 1993). By comparison, sediment from the access channel (TR-20) has a weak magnetic signal likely associated with dissolution of detrital ferrimagnetic particles in less oxygenated and more organic-rich sediment (e.g., Roberts, 2015), because the site is located further away from fluvial input to the harbour.

2.3 High-Resolution Analyses

Magnetic, physical, and mineralogical analyses of core CPS1 were undertaken at high-resolution on whole core sections, on half-core split surfaces, on continuous u-channels (2 cm x 2 cm x core length), and on a series of discrete samples (Table 1). The discrete samples are a series of 50 standard 8 cm^3 cubes (2 cm x 2 cm x 2 cm) that were used for magnetic analysis and ca 5 g of sediment that was used for mineralogical analysis, taken at ca 10 cm intervals down-core (see sampling strategy log in Fig. 2). This discrete sampling interval is comparable to the highest sampling resolution previously achieved in Portus.

2.3.1 Physical Properties

CT-scan images and gamma ray attenuation provide indications of sediment density. They are measured rapidly at high-resolution and are non-destructive (St-Onge et al., 2007; Fortin et al., 2013). CT-scan images of whole cores was obtained at the *Institut national de la recherche scientifique Eau-Terre-Environments* (INRS-ETE) using a Siemens SOMATOM Definition sliding gantry CT-Scanner. Tomograms were acquired continuously with a pixel size of 0.06 cm and were then transferred into digital format using a standard Hounsfield scale (Hounsfield, 1973). Higher density and higher atomic numbers generate greater X-ray attenuation, which is represented by higher CT number and lighter tones on a CT scan image. Gamma ray attenuation was measured on whole cores at 1-cm intervals using a Cesium-137 gamma ray source and detector mounted on a multi-sensor core logger (MSCL; Geotek Ltd.) at ISMER, UQAR. Imaging of half-core split surfaces was done using a linescan imaging Geoscan IV (Geotek Ltd) instrument.

2.3.2 Magnetic Properties

Magnetic mineral assemblages in the sediment were characterised using room-temperature magnetic properties, including the magnetic susceptibility, NRM and laboratory-induced magnetisations, and coercivity-dependent parameters. Magnetic susceptibility primarily reflects ferrimagnetic mineral concentration and is influenced by sediment composition, magnetic mineralogy, and grain size. The volume magnetic susceptibility (κ) was measured on the whole cores using a Bartington Instruments MS2C loop sensor at 1-cm stratigraphic intervals, and then on the half-core split surface with a MS2E high-sensitivity point sensor at 0.5-cm stratigraphic intervals at ISMER. Frequency-dependent magnetic susceptibility ($\chi_{FD\%}$) of cube samples was measured using a MS2B dual frequency sensor at The Australian Archaeomagnetism Laboratory (TAAL), La Trobe University. $\chi_{FD\%}$ is defined as $\chi_{FD\%} = (\chi_{LF} - \chi_{HF}) / \chi_{LF} \times 100$, with low and high frequencies (LF and HF) of 0.46 and 4.6 kHz, respectively (Dearing, 1999). $\chi_{FD\%}$ is controlled by the grain size distribution of superparamagnetic (SP) and stable SD particles (Eyre, 1997). Measurements were repeated at least six times; average values and standard errors are reported.

The NRM and ARM were measured and stepwise demagnetised on u-channels from 0 to 100 mT in 13 and 5 steps, respectively, using a 2-G Enterprises cryogenic magnetometer for u-channels at ISMER. ARM was imparted in a peak AF of 100 mT with a direct bias field of 0.05 mT. κ_{ARM} is the ARM normalised by the direct bias field. Principal component analysis (PCA) of NRM demagnetisation data was performed using the Puffin Plot software (Lurcock and Wilson, 2012). Four data points were masked at section ends to account for the width of the response function of the cryogenic magnetometer pick-up coils (Weeks et al., 1993) and data from intervals with incompletely filled u-channels or gaps were removed. The median destructive field (MDF) is the AF required to demagnetise half of the initial remanence. MDF is a coercivity indicator and is a useful grain size indicator when the magnetic mineral assemblage is uniform (Dankers, 1981;

Dunlop and Ozdemir, 1997). Like κ, ARM is controlled mainly by the concentration of ferrimagnetic particles. In addition, SD grains more easily acquire ARM than coarser multi-domain (MD) grains (Maher, 1988; Evans and Heller, 2003), so ARM is also a useful magnetic grain size indicator (i.e., κ_{ARM}/κ, MDF_{ARM}).

Hysteresis loops, IRM acquisition curves, and backfield demagnetisation curves were measured for each sample in a maximum field of 1 T using a Princeton Measurement Corp. vibrating sample magnetometer at the Australian National University (ANU). The bulk coercive force (H_c), the remanent coercive force (H_{cr}), the saturation magnetisation (M_s), and the saturation remanence (M_r) were obtained and the ratios M_r/M_s and H_{cr}/H_c are used as magnetic grain size indicators (Day et al., 1977). The hard isothermal remanent magnetisation (HIRM = (IRM_{1T}+$IRM_{-0.3T}$)/2; King and Channell, 1991) and the S-ratio (S-ratio = -IRM_{-300mT}/SIRM; Stober and Thompson, 1979) were calculated; they reflect the absolute concentration of high coercivity magnetic minerals and the relative concentration of low to high coercivity minerals, respectively (Liu et al., 2012). $B_{1/2}$ is half the applied field required for a sample to reach saturation and reflects the ease with which a sample is magnetised; it is a coercivity indicator. The 50 measured IRM acquisition curves were unmixed using an unsupervised approach (Heslop and Dillon, 2007) to identify and characterise the end-members that represent magnetic grain populationsFinally, first-order reversal curve (FORC; Roberts et al., 2000) diagrams for seven samples (CPS1-3-7, 4-5, 4-11, 5-5, 5-8, 6-8, and 7-3) were obtained using the same instrument to further explore the magnetic coercivity spectrum, domain structure, and magnetic interactions of different sediment types.

2.3.3 Granulometry

After completion of magnetic analyses, sediments in cube samples were air-dried at room temperature. To prepare samples for grain size analysis, dried sediments were sieved through a 2-mm mesh and were gently homogenised using an agate mortar and pestle. Subsamples of about 2 g were treated repeatedly with hydrogen peroxide (H_2O_2) and gentle heating to remove organic matter, until peroxide addition to the sediment did not react further. Finally, sediment dispersion of the treated and rinsed samples was achieved by adding 1 mL of 0.5M sodium hexametaphosphate ($NaPO_3$) and ultrasonicating for 15 minutes. Grain size analyses were performed using a Malvern Mastersizer 2000 laser diffraction spectrophotometer at the Australian Nuclear Science and Technology Organisation (ANSTO). Each prepared sample underwent three successive 10-second measurement runs using continuous sonication to disperse aggregated particles. All statistical grain-size parameters were calculated with the GRADISTAT software (Blott and Pye, 2001) using the Folk and Ward graphical method (Folk and Ward, 1957). Logarithmic biplots of the median (D50) and 90^{th} percentile diameter (D90) or the Passega diagram (Passega, 1964; Bravard and Peiry, 1999) were used to estimate the hydrodynamic energy associated with sediment deposition from decantation to rolling.

2.3.4 Bulk and Clay Mineralogy

Before mineralogical analysis, the detrital sediment fraction of the samples was isolated using 10 mL of peroxide (30% H_2O_2) and 10 mL of hydrochloric acid (0.5M HCl) to remove organic matter and biogenic carbonate, respectively. Deflocculation was achieved by successive washings with distilled water. Next, for bulk mineralogy, sediment samples were ground with a McCrone micronizing mill with agate grinding elements for 5-10 min with 10 mL of ethanol to obtain a consistent grain size of <10 μm. The slurry was oven dried overnight at 60°C and was slightly homogenised with an agate mortar to avoid agglomeration of finer particles during drying. Random powder samples were analysed by X-ray diffraction (XRD) using a PANalytical X'Pert Powder diffractometer (copper anode; 45 kV; 40 mA intensity). Samples were scanned from 5° to 65° two-theta in steps of 0.020° two-theta and a counting time of 2 seconds per step.

For semi-quantification of major mineralogical components, bulk sediment XRD scans were processed using the software package X'Pert High-Score Plus (PANalytical) with Rietveld full-pattern fitting. This method permits semi-quantification of whole-sediment mineralogy with a precision of 5–10% for phyllosilicates and 5% for grain minerals. Major mineralogical components quantified by this technique are quartz, K-feldspar, plagioclase feldspar, pyroxene, magnetite, pyrite, and phyllosilicates. The sum of quartz, phyllosilicates, K-feldspar, and Na-plagioclase contents is a detritus index that reflects changes in detrital influx or terrigenous supply (e.g., Keller and Pardo, 2004; Mort et al., 2008; Montero-Serrano et al., 2015). The ratio of fine detrital material (phyllosillicates) to coarse detrital material (quartz, plagioclases, and K-feldspars) is denoted Phy/(Qz+Pl+Feld) and indicates hydrodynamic sorting intensity.

Clay-mineral associations (smectite, illite, kaolinite, and chlorite) were studied using XRD following the protocols of Bout-Roumazeilles et al. (1999) and Montero-Serrano et al. (2009). The clay fraction was separated by settling according to Stokes's law, concentrated by centrifugation, and oriented by wet smearing on glass slides. Analyses were run from 2.49° to 32.49° 2θ on a PANalytical X'Pert Powder diffractometer. Three runs were made after air-drying each sample with ethyleneglycol vapour saturation for 12 hours and heating at 490°C for 2 hours. Each clay mineral is characterised by its basal layer plus interlayer interval (d) from XRD analysis (Brown and Brindley, 1980). Semi-quantitative clay mineral abundance estimation (smectite, illite, chlorite, and kaolinite), based on peak areas, was performed using the MacDiff® 4.2.5 software (Petschick, 2000). The reproducibility of measurements is estimated to be 5% for each clay mineral, as checked by replicate sample analysis.

2.3.5 Radiocarbon dating

Radiocarbon dating was performed using an Accelerator Mass Spectrometry (AMS) at ANSTO (Fink et al., 2004). Six samples of short-lived terrestrial material were measured, including three seeds, one coniferous bud, and two pollen/charcoal samples (Table 2). Measured ages were calibrated using the ^{14}C calibration program CALIB 7.0 (http://calib.qub.ac.uk/calib/calib.html; 1.0 (Stuiver et al., 2017) and the IntCal13 dataset (Reimer et al., 2013) and are stated using 2 sigma errors. The pollen extraction by density separation with lithium heteropolytungstate (LST) heavy liquid revealed abundant charcoal in the two pollen samples, and charcoal could not be separated from the pollen prior to dating. The dated carbon for samples OZS598 and OZS602 must, thus, come from both pollen and charcoal with possibly different respective ages. This was taken into account using Bayesian age modelling with the Charcoal Outlier Model in OxCal v4.2.3 (Bronk Ramsey and Lee, 2013), with an overall agreement of 93%. This model considers sample types and for the two pollen samples that also incorporated charcoal, outliers to older times are allowed to account for possible older wood in charcoal. The same radiocarbon calibration and age modelling method was applied to previously published radiocarbon dates from Portus cores TR14 (Delile et al., 2014) and CT1 (Salomon et al., 2012).

3. RESULTS

3.1 Stratigraphy

Six sedimentary units, labelled A to F from base to top, are defined based on lithology from core descriptions, photos, CT-scanning, density (gamma-ray attenuation and CT-number), magnetic susceptibility, and physical grain size data (Fig. 2). These units are described as follows.

3.1.1 Unit A

Unit A occurs at the base of the core (696 cm) to 573 cm and is composed of laminated yellow muddy sands characterised by relatively high density and magnetic susceptibility values (Fig. 2). Grain size analysis of four discrete samples indicate unimodal distributions and mean grain size ranging from 47 to 119 µm. The upper 10 cm has fine laminations of sandy muds and muddy sands. A sharp oblique discontinuity cuts these laminations and marks the end of unit A. Unit A has relatively high quartz content (up to 45%), coarse detrital material (Phy/(Qz+Pl+Feld)), and virtually no pyrite or pyroxene (Fig. 3). The magnetic particle assemblage is dominated by low coercivity minerals, as indicated by saturation of the IRM below 300 mT, which results in S-ratio values close to one and low HIRM values (Fig. 3). The low-coercivity magnetic component EM1 has the highest relative contribution in unit A, reaching 86% of the IRM (Fig. 3).

3.1.2 Unit B

Unit B is identified from depths of 573 to 480 cm and is composed of massive sands and muddy sands with cm-sized mud clasts. Immediately above the sharp oblique discontinuity at 573 cm is a 38-cm-thick massive medium sand layer with unimodal grain size distribution (mode 340 µm; sample 7-1; Fig. 2E) that encompasses the coarsest mean grain size in the studied core CPS1 (291 µm; sample 7-1; Fig. 2E). At 535 cm, a sharp κ drop of one order of magnitude and an increased mud content marks a change from sand to muddy sand (Figs. 2C-D). The muddy sand has a bimodal grain size distribution, with a first mode similar to the massive sand (341 µm) and a much finer second mode of 39 µm (each mode is calculated from 4 samples). Sample 6-8 was taken from an individual mud clast within the muddy sands and is a distinctly finer medium silt with mean grain size of 8 µm (Fig. 2E). Unit B is clearly composed of ungraded reworked sediments. This unit is capped with fine laminations of very coarse silts (mean grain size of 47 µm; sample 6-5). The mineralogical and magnetic properties in the massive sands of unit B are similar to these of unit A. In contrast, the muddy sands with mud clasts in unit B have relatively lower quartz content (30 to 34%), finer detrital minerals (Phy/(Qz+Pl+Feld)), and higher pyrite (0.5 to 1.4%) contents (Fig. 4). The magnetic component EM2 appears in unit B and reaches maximum values in mud clast sample 6-8 (Fig. 4).

3.1.3 Unit C

Unit C from 480 to 414 cm is composed of graded beds of muddy sands and sandy muds intercalated with a 30-cm-thick central layer (430-460 cm) of abundant cm-size rocks, ceramic fragments, wood, and other organic debris. A sharp change in gamma ray attenuation and CT-number at 480 cm (Fig. 2A-B) reflects the distinct densities of sedimentary units B and C. The grain size distributions of the six discrete samples from unit C reveal, from base to top, a coarsening upward sequence and a fining upward sequence. Similarly, the concentration of ferrimagnetic minerals as indicated by κ, M_s, ARM, and NRM increases steeply from the base of unit C to the debris layer, and decreases gradually to the top of unit C. The three samples within the debris layer have trimodal grain size distributions with the coarser mode reaching 590 µm (Fig. 2E). In contrast, samples below and above the debris layer have bimodal distributions (224 and 6 µm). Mineralogical and magnetic properties have sharp and large amplitude changes in the debris layer of unit C. Notably HIRM, magnetic component EM1, and the pyroxene content reach peak values (Fig. 3). In addition, paleomagnetic inclinations depart markedly from the expected value for a geocentric axial dipole (GAD) field at the latitude of the coring site. Instead of dipping 61° below the horizontal plane, the magnetic inclination is flattened horizontally and has reversed polarity.

3.1.4 Unit D

Unit D is from 414 to 165 cm and is the thickest and most homogenous sedimentary unit of core CPS1. The base of unit D is characterised by a sharp increase in mud content from 44% (sample 5-8 at 423 cm in unit C) to 86% (sample 5-7 at 413 cm in unit D). Overall, unit D has lower amplitude variations in density, magnetic susceptibility, and mud content (Fig. 2). Two sub-units D1 (414-220 cm) and D2 (220-165 cm) are identified. D1 is composed of medium silts with average grain size of 13 ± 3 µm (19 samples) and unimodal grain size distributions (Fig. 3E). D1 has virtually no particles bigger than 2 mm. In contrast, sub-unit D2 (6 samples) has particles over 2 mm and organic debris, it is composed of coarsening upward coarse to very coarse silts with average grain size of 30 ± 4 µm, and grain size distributions are bimodal at the base and trimodal at the top (Fig. 2E). Unit D has distinctively finer detrital minerals (Phy/(Qz+Pl+Feld)), relatively higher pyrite and gypsum contents, and lower S-ratios than the other units (Fig. 3), and there are three magnetic grain populations (Fig. 4). The two sub-units have remarkably different mineralogy and magnetic properties. The detrital minerals are much coarser in sub-unit D2 than D1, and the quartz content increases from 29% to 36% (Fig. 3). Sub-unit D2 has peak values of HIRM, EM1, and pyroxene; the same signature occurs in the debris layer of unit C and is found in overlying unit E (Fig. 3). Moreover, in sub-unit D2 the magnetic grain size indicators M_r/M_s, H_{cr}/H_c, MDF_{ARM}, χ_{FD} (Fig. 5) and the open shape of hysteresis loops (supplementary material 3) all indicate smaller ferrimagnetic grains.

3.1.5 Unit E

Unit E from 165 to 50 cm is composed of abundant potshards and shell fragments, rocks, and organic debris associated with large amplitude changes in density, magnetic susceptibility, and mud content (Fig. 2). The irregular surface of the debris-dominated unit E prevented the use of the multi-sensor core logger for core section 2. U-channel sampling was also impossible with many debris pieces being larger than the u-channel width (2 cm). Nevertheless, the four discrete sediment samples analyzed for granulometry are coarse silts to fine sands with highly variable average grain size (ranging from 23 to 158 µm) and uni- to tri-modal grain size distributions. Magnetic mineralogy and grain size are also variable (Figs. 3 and 5). There is a trend toward finer detrital minerals and the pyrite content decreases sharply to minimum values (Fig. 3). Magnetic component EM2 has maximum values (Fig. 4), with χ_{fd} values from 3 to 7 being indicative of fine SD and SP grains.

3.1.6 Unit F

The uppermost unit F from 50 to 0 cm is composed of silts with a color transition from yellow to brown. The yellow mud has unimodal grain size distribution and average grain size of 9 µm (sample 1-2; Fig. 2E). The brown mud has a trimodal distribution and average grain size of 19 µm (sample 1-1). Magnetic component EM1 dominates with values up to 79%, similar to unit A.

3.2 Magnetic Mineral Assemblage

Magnetic properties provide information about the nature, source, and transportation of magnetic particle populations in a sediment. The studied bulk sediment is dominated by low coercivity magnetic minerals, as indicated by IRM saturation in fields below 300 mT (Fig. 4). FORC diagrams (supplementary material 3) and $\chi_{FD\%}$ values (Fig. 5) indicate a mixture of SD, MD, and SP domain states. MDF_{ARM} has the same general down-core trend as $\chi_{FD\%}$ and values (32 to 40 mT) are consistent with those of detrital and low coercivity biogenic magnetic minerals (Egli, 2004). Ultrafine SP particles form commonly in soils and by burning (Evans and Heller, 2003; Herries, 2009), the latter being likely in Portus from cooking and heating.

Unmixing analysis of 50 IRM acquisition curves (Heslop, 2015) indicates that there are three end-members (EM1, 2 and 3; Fig. 4) with the fit yielding an R^2 value of 0.988. The three magnetic subpopulations EM1, EM2, and EM3 have coercivities ($B_{1/2}$; Fig. 4) of 21, 31, and 11 mT, respectively. The proportion of the higher coercivity population EM2 is greater in muddy sediments (units C, D, E), while the intermediate coercivity EM1 component has peak values in sandy deposits (units A, B, F). Peak concentrations of EM1 also correspond to lower relative contributions from the other magnetic component (Fig. 4), which hints at a sudden input of EM1. Moreover, EM1 peaks are associated with peak pyroxene contents (Fig. 3), which likely come from basalts in the Tiber River catchment; peak HIRM values (Fig. 3) may also correspond to inputs of these volcanic grains, or to pedogenic magnetic minerals such as goethite and hematite brought by runoff. Altogether, the magnetic properties suggest that EM1 corresponds to detrital magnetic minerals of fluvial origin and that EM2 corresponds to biogenic magnetic minerals from the harbour. The lowest coercivity population EM3 is present in lower proportions (generally < 30%; Fig. 4), with higher absolute values in the sands of units A and B (not shown), and hysteresis loops, coercivity ratios, and remanence ratios indicative of MD magnetic minerals.

3.3 Chronology

Radiocarbon dating, calibration, and Bayesian depth-age modelling reveals two distinct periods in core CPS1 (Fig. 6; Table 2). The first period corresponds to sandy unit A in the lower portion of the core and has one date (calibrated 765-492 BC; modelled 764-434 BC). The second period corresponds to homogeneous muddy unit D (414-165 cm) and comprises four dates between cal AD 28 and AD 311. Another date from the upper part of the high-energy flow deposit (unit C) is derived from extracted pollen/charcoal (sample OZS598) and gives a large modelled age uncertainty (Table 2) because of the presence of charcoal from burnt material with a possible inherited age. Sub-centimeter-sized ceramic fragments in the central layer of the high-energy flow deposit (unit C) indicate human activity and provide some chronological insight. The small ceramic fragments have similar color and texture to those in the uppermost debris layer (unit E) that caps the harbour deposit (unit D).

The four dates in homogeneous unit D reveal rapid sediment deposition during the Roman Empire. The calibrated radiocarbon dates fall within the interval cal AD 28 – AD 311, and Bayesian age modelling, which takes into account the type of dated material, gives slightly younger probable dates and a larger age interval AD 128 – AD 616 because the uppermost sample OZS602 consists of a pollen/charcoal mixture (Table 2; Fig. 6). The radiocarbon-based chronology of unit D assumes constant sedimentation rates (linear interpolation) between the median modelled ages (Table 2) and suggests deposition over 165 years during the second and third century AD, at average sedimentation rates of ~1 cm per year (Fig. 6B). The true harbour deposition period could be shorter or longer than suggested by age modelling because of the uncertain uppermost date. The harbour deposit period is short relative to radiocarbon dating and calibration errors, and therefore the radiocarbon-based chronology cannot be used to date historical events. Instead, the core CPS1 chronology provides a detailed sequence of events. Each cm of muddy unit D in core CPS1 integrates on average less than one year, and each cube sample no more than 2 years.

4. DISCUSSION

4.1 High-resolution chronostratigraphy of core CPS1

The often complex stratigraphy of ancient Roman harbours (e.g., Hadler et al., 2015; Finkler et al., 2017) can be simplified to a three-unit sequence: a pre-harbour deposit, a harbour deposit, and a post-harbour or abandonment deposit (e.g., Goiran and Morhange, 2001; Marriner and Morhange, 2007). The same general stratigraphy is reported here from the first stationary piston core recovered from Portus, and the new core chronostratigraphy is interpreted based on high-resolution multi-proxy analysis, age modelling, and historical context.

In core CPS1, the *pre-harbour deposit* corresponds to unit A and consists of stratified fluvio-coastal sediments. The smaller grain sizes and fine laminations in the upper part of unit A indicate calmer hydrological conditions possibly associated with a fluvial or lagoon environment. The radiocarbon-dated seed from the uppermost laminations of unit A yield an age (Table 2; Fig. 6A) consistent with previous geomorphological and stratigraphic studies that indicate that the Tiber River mouth was located near the site in the first millennium BC (Bellotti et al., 2011; Giraudi et al., 2009).

The *harbour deposit* consists of unit D and covers a continuous period of about one and a half centuries (Fig. 2B). The distinctive sedimentological signature of the harbour deposit relative to the natural pre-harbour deposit is evident from granulometry, physical and magnetic properties, bulk sediment, and clay mineralogy data (Figs. 2, 3, 4). The harbour deposit in the man-made Canale Traverso is characterised by greater mud content and finer detrital minerals (Fig. 3) that indicate a calmer, more isolated depositional environment. Relatively higher pyrite contents, lower ferrimagnetic mineral concentrations (lower κ, M_s, NRM, ARM), and the presence of biogenic magnetite (EM2; Fig. 4) indicate a more organic-rich deposit and more hypoxic conditions. An age for the start of the harbour deposit in Canale Traverso core CPS1 is obtained by interpolation and is modelled at AD 120 – AD 186 (Fig. 6). This age estimate suggests that the onset of harbour deposition in core CPS1 followed the massive enlargement and reorganization of Portus by Trajan that was completed by AD 117 (Keay et al., 2005). However, it is believed that Canale Traverso was built earlier, during the first century AD, as part of the initial Claudius harbour construction. This is based on the hypothesis of Testaguzza (1970) who suggested that the Darsena, Canale Traverso, and Fossa Traiana formed a complex built at the same time, and on the radiocarbon chronology of Canale Traverso core CT1 that contains sediment from the first century (Salomon et al., 2012). If the Canale Traverso was built during the first century AD, the age of the basal harbour deposit in core CPS1 does not date construction of Canale Traverso, but rather indicates that dredging operations removed about one century of previous harbour deposit. This issue is considered in section 4.3. The modelled age for the end of harbour deposit is obtained by interpolation at AD 164 - AD 643 (Fig. 6). The large age interval is inherent to the nature of the dated material (charcoal-rich pollen sample OZS602). Nevertheless, the modelled age interval AD

177 - AD 436 is obtained if sample OZS602 is not considered and a constant sedimentation rate is assumed from sample OZS601 to the top of the harbour sequence (Fig. 6).

Units E-F represent the *post-harbour deposit*. Accumulation of debris (unit E) into Canale Traverso marked the end of its use as a waterway. Uppermost unit F includes floodplain deposits and the recent soil deposit. What stands out in the stratigraphy of core CPS1 are the two consecutive reworked deposits (units B and C) located between the pre-harbour and harbour deposits. For the first time at Portus, reworked layers are identified precisely using high-resolution core scanning and multi-proxy analyses. Units B and C are discussed in more detail below.

4.2 New Chronostratigraphic Marker

The estimated end of harbour deposition in Canale Traverso is consistent with dates from cores S13 and TR14 located downstream in the access channel (70 m and 170 m distance from CPS1; Fig 1B), but is significantly younger than in core CT1, which is located upstream toward Fossa Traiana (130 m distance from CPS1; Fig. 1B). Based on grain size data in core CT1, Salomon et al. (2012) reported two distinct harbour deposits; one with low Tiber River influence and one with high Tiber River influence (Fig. 7; Salomon et al., 2012). Our pilot magnetic analysis supports this stratigraphy with a distinct magnetic mineral assemblage in the core CT1 high Tiber River influence deposit and similar magnetic assemblages for the CT1 low Tiber influence deposit and core TR20 from the access channel (supplementary material 1). The sudden change in CT1 sediment type corresponds to a sharp κ increase, which can be correlated to a similar sharp κ increase at a similar median modelled age in core CPS1 (Fig. 7). While the sharp κ increase in core CT1 likely corresponds to increased river transport of ferrimagnetic detrital particles, the sharp κ increase in core CPS1 corresponds to the debris layer (unit E; Fig. 2), which also has large amplitude changes attributed to abundant ceramic fragments, rocks, and overall heterogeneous debris having highly variable magnetic properties. At a similar modelled age in core TR14, a sudden onset of marine influence is evident in the access channel based on geochemistry data (Fig. 7; Delile et al., 2014). Core CPS1 is located between cores TR14 and CT1 and, thus, provides a link for correlating the Portus cores.

Damming of Canale Traverso with debris at the junction of the access channel (site CPS1) would have blocked river input into the harbour basins, changing predominantly fluvial to marine influence in the access channel (TR14), and increasing river influence upstream of Canale Traverso (CT1). Combining age modelling, κ records, and previous grain size and geochemistry studies (Salomon et al., 2012; Delile et al., 2014) reveals a new chronostratigraphic marker at Portus at the time Canale Traverso was decommissioned. This change may correspond to Portus becoming a town in the 4th century when the immediate vicinity of Canale Traverso changed its function from administrative to residential (Keay et al, 2005; Paroli, 2005).

4.3 Reworking of Sediments into a Roman Canal

4.3.1 The Dredged Deposit

CT scan and digital images clearly reveal an oblique erosional contact that cuts natural laminated deposits and is overlain by 93 cm of sands with angular mud clasts in the upper part (unit B; Fig. 2). The sands deposited before and after the oblique contact have similar physical, mineralogical, and magnetic properties (Figs. 2, 3, 4, 5), which suggests that the reworked unit B was sourced locally. The presence of rectangular-shaped mud clasts with immature texture (Lie et al., 2017) further indicates a local mass movement event such as a river bank collapse, a landslide or debris flow, possibly triggered by human activities or an earthquake. However, observed immature mud clasts embedded in much coarser sands imply a local source of mud deposited in a calm environment and a local source of sands deposited in a vigorous hydrodynamic environment. Contemporaneous mud and sand deposits within a small fabricated canal appears unlikely, and a local mass movement is unlikely to explain the oblique erosive contact in the canal center. Another hypothesis is a weather-related event such as storm, tsunami or flood. Such high-energy events have been reported in the nearby Ostia harbour (Goiran et al., 2014; Hadler et al., 2015); whilst event deposits in Portus are reported here for the first time, the river influence at Portus is well-documented (Goiran et al., 2010; Delile et al., 2014; Salomon et al., 2012; 2014). A flood appears likely; however, a high-energy flow is inconsistent with the ungraded sands and immature mud clasts of unit B, which rather point to low velocity flow. A more likely explanation is that unit B corresponds to an admixture of coastal sands and harbour mud that were shoveled locally and dropped into place, forming a dredged deposit (Table 3; Fig. 8). Multi-proxy analyses of the mud clast (sample 6-8) indicate contrasting magnetic and physical properties with the later harbour mud of unit D, which points to different depositional conditions before and after dredging. The differences include distinctively higher S-ratio and higher EM2 biogenic proportion in the mud clast (Figs. 3, 4), and the lowest D50 value of core CPS1, with the grain size of sample 6-8 plotting in the lower energy or decantation end of Figure 5F. It is, thus, possible that dredging was performed at the time of the major Trajan work, which drastically changed the harbour infrastructure (Keay et al., 2005) and hydrodynamics (Millet et al., 2014).

Further support for calm hydrodynamic conditions at the time of deposition of unit B comes from the paleomagnetic inclination. Muddy sands in upper unit B have a strong, stable, and well-defined magnetic remanence with inclination values near the GAD field value for the latitude of Portus (Figs. 9D, 10). In unit B, three distinct magnetic particle populations (Fig. 4) form a single magnetization component, which indicates that a detrital remanent magnetisation (DRM) acquisition process at about the time of deposition is more likely than a chemical remanent magnetisation (CRM) that would have happened anytime later. Additional support for a DRM comes from the predominance of biogenic particles in the supposedly dredged deposit because such particles are small and readily undergo chemical alteration. Such rapid remanence acquisition within an event deposit resembles redeposition experiments of slurries with low water content (Barton et al, 1980) and adobe brick fabrication, where clay and water mixtures rapidly acquire a shear or shock remanent magnetisation when thrown into a mould (Games, 1977; 1983). The paleomagnetic results, thus, indicate limited resuspension of slurry material and calm hydrodynamic conditions at the site, which further supports the suggested dredged deposit interpretation for unit B.

4.3.2 The Hyperpycnal Deposit

Immediately overlying the dredged deposit (unit B) is another reworked deposit of 66 cm thickness (unit C), which is composed of a coarsening upward basal sequence, a 30 cm-thick central debris layer, and a fining upward top sequence. Unit C is a typical hyperpycnite that results from high-energy flow that sorts particles into a coarsening sequence during the waxing stage of the flow, and a fining upward sequence during the waning stage of the flow (Mulder, 2003; Fig. 8). The hyperpycnal deposit in core CPS1 is readily identifiable using grain size, bulk mineralogy, and magnetic data (Fig. 10). In addition to grain size sorting, flattened paleomagnetic inclinations (Figs. 9C and 10) are an indicator of high-energy deposits (St-Onge et al., 2004). The distinct sedimentary properties of the central debris layer provide a clear river input signature, particularly using the fluvial magnetic component EM1, the content of high coercivity minerals (HIRM) and pyroxenes, and a higher smectite/(illite+chlorite) ratio (Fig. 3). Coeval peak values of these parameters in the debris layer point to a common fluvial source and transport mechanism for different types of detrital material.

Hyperpycnal deposits in natural environments are associated with dense water flowing into less dense water, the most typical example being sediment-laden river floodwaters plunging into the sea (Mulder et al., 2003). Catastrophic drainage events such as glacial outburst flood and dam-breaks can also generate hyperpycnites (e.g., St-Onge et al., 2004; Mulder et al., 2009; Mulder and Chapron, 2011; Duboc et al., 2017). To our knowledge, this is the first report of a hyperpycnal deposit in a fabricated structure. How did a hyperpycnite form in Canale Traverso? Did the high-intensity flow have natural causes, such as in association with a river flood, storm, or tsunami event, or was it human-induced such as through opening of a canal gate, or from dredging? The hypothesis of a major river flood is ruled out by the presence of a thick central debris layer in unit C. While a typically steady and sustained flood flow carries a suspended load over hours to weeks, the debris layer of unit C instead indicates bedload transport during a short-duration high-energy flow. Tsunami or extreme storm waves are high-energy, short-duration events that form graded deposit with debris (Robke and Vött, 2017). A single fining upward sequence (waning flow) is typically reported for such events, but the coarsening upward sequence (waxing flow) observed in Canale Traverso could have been generated by inflow and backflow events from the sea, travelling in the harbour basins, and up the canals. However, there is no erosive contact at the base of unit C as may be expected for a tsunami, the debris layer has a clear fluvial signature (Table 3), and previous combined geophysical surveys, sedimentological, macro- and microfossil, and geochemical analyses have not revealed a tsunamite in Portus (Delile et al., 2014; DiBella et al., 2011; Goiran et al., 2010; Pepe et al., 2013; Sadori et al., 2010; Salomon et al., 2012; 2014).

Assuming that the deposit tracked the flow hydrograph, the presence of debris and an erosive contact are key to identifying the type of flow and the conditions under which the hyperpycnite formed (Mulder, 2003). According to Mulder (2003), the debris layer located below the fining upward sequence and the absence of an erosive basal contact in unit C best correspond to a natural dam-break event. Erosion of a natural sediment dam appears to be a good analogue for opening a canal gate in a Roman harbour context. Opening Canale Traverso would have suddenly increased water flow from the river (waxing flow; Fig. 8), eroding and transporting sediment and debris that would have blocked the canal, or accumulated on the river side of the gate, and then water flow would have decreased (waning flow; Fig. 8) until steady flow is reached. Another hypothesis is a dredging-generated hyperpycnal deposit, where the fining upward sediment would be deposited by suction under the dredging shovel. However, absence of an erosive contact between units B and C does not support this idea, which also does not account for the coarsening-upward and debris layers (Table 3). Based on multi-proxy sediment analysis and high-resolution stratigraphy, our preferred interpretation for unit C is a canal dam-break hyperpycnal deposit (Fig. 8), which is an analogue for natural dam-breaks in a fabricated structure.

4.3.3 Event deposits summary

Units B and C are consecutive event deposits. Our multi-proxy data set suggests that the event deposits were human-induced, with our preferred interpretation of unit B being a dredged deposit, and unit C being a canal dam-break hyperpycnal deposit (Table 3). The flood, tsunami or storm hypotheses are plausible alternative interpretations for unit C, which was deposited under high-energy hydrodynamic conditions. The hypothesised dredging event may have occurred during the Trajanic redevelopment (AD 112-117) (Keay et al., 2005), based on age modelling and the presence of different muds in the harbour deposit (unit D) and in the dredged deposit (mud clast sample 6-8). Sediment mix and drop during dredging would have formed the dredged deposit, while waxing and waning flows would have formed the hyperpycnal deposit (Fig. 8). For the first time, major event deposits are described in Portus, and identification of a 159-cm-thick reworked sediment has important implications for age-depth modelling and water depth reconstructions. The Palaeoenvironmental Age-Depth Model (PADM) chart (Fig. 6A; Salomon et al., 2016) indicates water depth based on core stratigraphy and reconstructed local relative sea level (Goiran et al., 2009). The water depth in Canale Traverso after dredging (top of Unit C) was about 3 m, which provides sufficient draught for ships 150 t and smaller, such as *Bourse de Marseille* and *Fiumicino 1* (Gassend, 1982; Pomey and Tchernia, 1978; Pomey and Rieth, 2005; Boetto, 2010).

4.4 Canal Gate Usage

Were canal gates used in Portus for flood control? Tiber floods in the early first century AD had silted the fluvial harbour of Ostia, which was then abandoned (Goiran et al., 2014; Hadler et al., 2015). It is probable that the Romans used canal gates for flood management in Portus considering that a main motivation for canal construction was to free Rome from flood dangers (AD 46 inscription - Thylander, 1952: B310 = CIL XIV 85 = ILS 207; and AD 102-109 inscription - Thylander 1952: B312 = CIL XIV 878 = CIL VI 964 = ILS 5797a; Keay et al., 2005). Canal gate technology was presumably used as early as the 3rd century BC by Ptolemy II in the Ancient Suez Canal, which was re-built by Trajan (Moore, 1950). The major redevelopment of Portus by Trajan in AD 112-117 (Keay et al., 2005) took place soon after a catastrophic Tiber flood as reported by Pliny the Younger in the winter of 108-109 AD (Syme, 1985). However, it is unknown if and how that flood impacted Portus. We now evaluate if multi-proxy analysis of the harbour deposit in core CPS1 (unit D) is consistent with canal gate use.

The hyperpycnal deposit has a clear fluvial input signature. Sub-unit D2 has a similar fluvial signature, with peak values of EM1, HIRM, pyroxene, and higher smectite/(illite+chlorite) ratio (Fig. 3). However, there are significant differences, including the absence of an erosive contact or discontinuity in D2, no grading, unchanged magnetic particle concentrations (Fig. 2), and no flattened paleomagnetic inclinations (Fig. 9A). These results indicate that D2 is not an event deposit, but rather a harbour deposit with marked river input over a period of about 60 years. Grain size, magnetic, and bulk mineralogical data clearly indicate increased sand content, increased fluvial magnetic particle populations (EM1), and coarser detrital minerals in D2 relative to the previous harbour deposit D1 (Fig. 3). The D90-D50 diagram also indicates greater hydrodynamic energy for D2 relative to D1 (Fig. 5F). These results are consistent with ostracod and pollen analyses, which indicate greater freshwater input in the upper part of the harbour sequence in core S5 (location on Figure 1; Sadori et al., 2010), as well as increased magnetic susceptibility in core TR14 (Figs. 1 and 7; Delile et al., 2014). Together, the results can be interpreted as: (1) sub-unit D2 being deposited in an open Canale Traverso configuration that connected the Tiber River and the harbour basins after a gate-controlled period (sub-unit D1), and/or (2) rapid climate change to wetter conditions and stronger fluvial impact in the early 3rd century AD. River input proxies for sub-unit D1 (Fig. 3) do not have coeval peak values. Only the clay mineral indicator has peak values such as in the hyperpycnal deposit and D2. It is possible that if the coarser grains tracked by EM1, HIRM, and pyroxene content were blocked from Canale Traverso by canal gates, finer clay particles may have flowed over the gates during flood events or reached the canal by local runoff in Portus. Overall, reduced river input in D1, sulphidic diagenetic conditions indicated by increased pyrite formation, and warmer and more saline conditions indicated by higher gypsum content (Fig. 3) are consistent with D1 being deposited under gate controlled conditions. The multi-proxy dataset provides abundant evidence in support of the idea of canal gate usage for water flow management.

The period of sub-unit D2 corresponds to the onset of Roman Empire contraction which is characterized by increased climate instability (Büntgen et al., 2011), political turmoil, cultural change, socio-economic instability (Duncan-Jones, 2006), and human health issues such as the large-scale Plague of Cyprian (AD 251-266; Vuorinen, 1997). Thus, climatic or socio-economic instabilities could possibly explain a sudden change in harbour management and canal gate operation, and the later decommissioning of Canale Traverso. The capacity to close the only inland waterway from the Tiber River to the capital city's harbour basins would undoubtedly have been advantageous during flood events and at times of war. The sedimentary archives in Portus have an undeniably strong anthropogenic influence; the depositional basin itself is man-made and the site has witnessed intense human activity. Core CPS1 provides evidence of over one and a half centuries of nearly annually-resolved harbour occupation at the height of the Roman Empire, with humans using technologies in response to natural environmental and societal stresses.

5. CONCLUSIONS

Multi-proxy and high-resolution sediment analysis, including piston coring, core scanning, grain size, paleo- and rock-magnetism, bulk and clay mineralogy, and radiocarbon dating was applied in an ancient harbour context to understand its history. This method revealed 159 cm of event deposits (units B and C) and 249 cm of harbour sediment (Unit D) in core CPS1. Without piston coring, a fine stratigraphy would not be preserved and it is likely that the suggested dredged deposit (Unit B) would be undiscernable from the pre-harbour deposit (unit A), and most crucially for water depth reconstruction, the 66-cm-thick hyperpycnal deposit (Unit C) would have been included in the harbour deposit (Unit D). Portus core correlation was achieved using magnetic susceptibility and age modelling, and a chronostratigraphic marker at the time Canale Traverso was decommissioned is proposed to reconcile previous core interpretations. Piston coring, whole core CT-scanning, and magnetic analyses have proven useful for event stratigraphy and geoarchaeology. Routine analysis of the type presented here could greatly improve chronostratigraphic analysis and water depth reconstruction of ancient harbour deposits.

Our works also provides rare insights into Roman harbour technologies. Dredging activity in Canale Traverso during the Trajanic-Hadrianic period (2nd century AD) provides a welle best-supported hypothesis for explaining unit B. The dredging event has not been reported previously and predates the known 4th century AD dredging depicted in a Roman epigraph. Portus was built in a delta, without bedrock that may hold direct evidence of canal gates. While future excavation of canal walls may provide direct evidence, this work provides indirect sedimentological indicators consistent with hypothesised canal gates at Portus, and supports the ideas of Testaguzza (1970) and Salomon et al. (2014). Magnetic analysis has been applied here to ancient harbour geoarchaeology for the first time. It has proven useful at Portus for core correlation (magnetic susceptibility), identification of event deposit (paleomagnetic inclination, κ_{ARM}/κ, IRM acquisition), and for providing a river input proxy (S-ratio, HIRM, IRM acquisition). Sedimentary magnetism is a versatile tool that can, therefore, be added to the geoarchaeologist's toolkit (Marriner and Morhange, 2007).

ACKNOWLEDGEMENTS

We thank Prof. Simon Keay and the *Soprintendenza Speciale per il Colosseo, il MNR e l'Area Archeologica di Roma, Sede di Ostia* for collaboration and access to the site; the drilling team of Guillaume Lopez, Régis Batteux, and Éric Semin (CETE Marseille); and Jacques Labrie and Alexandra Leclerc for laboratory work at ISMER and INRS-ETE. Thanks to the editors and reviewers for invaluable and constructive reviews. This work was supported by a postdoctoral fellowship of the *Fonds de recherche du Québec pour la nature et les technologies* (FRQNT) and La Trobe University Transforming Human Societies RFA and DVCR Research Fellowships to A. Lisé-Pronovost, and by the Natural Sciences and Engineering Research Council of Canada (NSERC) Discovery grants to G. St-Onge and J.-C. Montero-Serrano. The Young Scientist Program of the Agence Nationale de la Recherche (ANR 2011 JSH3 002 01) and the European Research Council ("Roman Mediterranean Ports program" under the European Union's Seventh Framework Programme – FP7/2007-2013 / ERC grant agreement n°339123) provided financial and logistical support. Fieldwork was supported by a Geological Society of America (GSA) graduate scholarship, and radiocarbon dating and particle grain size analysis were supported by a research grant from the Australian Institute of Nuclear Science and Engineering (AINSE ALNGRA15016) to A. Lisé-Pronovost. We also acknowledge the help of radiocarbon laboratory staff and financial support for the Centre for Accelerator Science at ANSTO, where the measurements were done, through the Australian National Collaborative Research Infrastructure Strategy (NCRIS).

REFERENCES

Allen, W., 1853. The Ancient Harbour of Seleucia, in Pieria. Journal of the Royal Geographical Society of London 23, 157-163.

Barton, C. E., McElhinny, M. W., Edwards, D. J., 1980. Laboratory studies of depositional DRM, Geophysical Journal of the Royal Astronomical Society 61, 355-377.

Bellotti, P., Calderoni, G., Rita, F.D., D'Orefice, M., D'Amico, C., Esu, D., Magri, D., Martinez, M.P., Tortora, P., Valeri, P., 2011. The Tiber River delta plain (Central Italy): coastal evolution and implications for the Ancient Ostia Roman settlement. The Holocene 21, 1105-1116.

Benito, G., Macklin, M. G., Zielhofer, C., Jones, A. F., Machado, M. J., 2015. Holocene flooding and climate change in the Mediterranean. Catena 130, 13-33.

Blott, S.J. and Pye, K., 2001. GRADISTAT: a grain size distribution and statistics package for the analysis of unconsolidated sediments. Earth Surface Processes and Landforms 26, 1237–1248.

Bockius, R., 2014. Künstliche Schifffahrtswege, Wasserbau und Hydrotechnische Einrichtungen im Altertum. In: P. Ettel/F. Daim/S. Berg-Hobohm et al. (Ed.), Großbaustelle 793. Das Kanalprojekt Karls des Großen zwischen Rhein und Donau. Mosaiksteine. Forschungen am Römisch-Germanischen Zentralmuseum 11 (Mainz 2014) 87–94.

Boetto, G. "Le Port vu de La Mer: L'apport de L'archéologie Navale À L'étude Des Ports Antiques." *Bolletino Di Archeologia Online* Special issue: XVII International Congress of Classical Archaeology, Roma 22-26 Septembre 2008 (2010): 112–28.Bout-Roumazeilles, V., Cortijo, E., Labeyrie, L., Debrabant, P., 1999. Clay mineral evidence of nepheloid layer contribution to the Heinrich layers in the Northwest Atlantic. Palaeogeography Palaeoclimatology Palaeoecology 146, 211–228.

Bravard, J.-P., and Peiry, J. L., 1999. The CM pattern as a tool for the classification of alluvial suites and floodplains along the river continuum. Geological Society London Special Publications 163, 259–268.

Bronk Ramsey, C., and Lee, S., 2013. Recent and Planned Developments of the Program OxCal. Radiocarbon 55 (2-3), 720-730.

Brown, G. and Brindley, G.W., 1980. X-ray diffraction procedures for clay mineral identification. In: Brindley, G.W., Brown, G. (Eds.), Crystal Structures of Clay Minerals and their X-ray Identification. Mineralogical Society, London, pp. 305–359.

Büntgen, U., Willy Tegel, W., Nicolussi, K., McCormick, M., Frank, D., Trouet, V., Kaplan, J. O., Herzig, F., Heussner, K.-U., Wanner, H. Luterbacher, J. Esper, J., 2011. 2500 Years of European Climate Variability and Human Susceptibility, Science 331 (6017), 578-582.

Camuffo, D. and Enzi, S., 1995. The analysis of two Bi-millenary series: Tiber and Po river floods. In: Jones, P.D., Bradley, R.S., Jouzel, J. (Eds.), Climatic variations and forcing mechanisms of the last 2000 years. NATO ASI Series, Series I: Global Environmental Change. vol. 41. Springer Verlag, Stuttgart, 433–450.

Coccia, F., 1993. Il “Portus Romae” fra tarda antichità ed altomedioevo. In L. Paroli and P. Delogu (Eds.), Storia economica di Roma nell’Altomedioevo alla luce dei recenti scavi archeologici. Firenze: Atti del Seminario di Roma, 183–188, “All’Insegna del Giglio.”

Dankers, P., 1981. Relationship between median destructive field and remanent co-ercive forces for dispersed natural magnetite, titanomagnetite and hematite. Geophysical Journal of the Royal Astronomical Society 64, 447–461.

Day, R., Fuller, M., Schmidt, V.A., 1977. Hysteresis properties of titano-magnetite: grain size and compositional dependence. Physics of the Earth and Planetary Interiors 13, 260-267.

Delile, H., Mazzini, I., Blichert-Toft, J., Goiran, J.-P., Arnaud-Godet, F., Salomon, F., Albarède, F., 2014. Geochemical investigation of a sediment core from the Trajan basin at Portus, the harbour of ancient Rome. Quaternary Science Reviews 87, 34-45.

Dearing, J.A., 1999. Environmental Magnetic Susceptibility: Using the Bartington MS2 System. Chi Pub., Kenilworth.

Duboc, Q., St-Onge, G., Lajeunesse, P. 2017. Sediment records of the influence of river damming on the dynamics of the Nelson and Churchill Rivers, western Hudson Bay, Canada, during the last centuries. The Holocene 27, 712-725.

Duncan-Jones, R. P., 2006. Economic change and the transition to Late Antiquity, In: Approaching Late Antiquity: The Transformation from Early to Late Empire, Eds. S. Swain, M. Edwards, Oxford Univ. Press, Oxford, pp. 20–52.

Dunlop, D.J., Özdemir, Ö., 1997. Rock Magnetism: Fundamentals and Frontiers. Cambridge University Press, Cambridge, New York.

Duchesne, M. J, Long, B. F., Labrie, J., Simpkin, P. G., 2006. On the use of computerized tomography scan analysis to determine the genesis of very high seismic reflection facies, *Journal of Geophysical Research* 111, B10103.

Egli, R., 2004. Characterization of individual rock magnetic components by analysis of remanence curves. 1. Unmixing natural sediments. Studia Geophysica et Geodaetica 48, 391-446.

Erol, O., and Pirazzoli, P.A.,1992. Seleucia Pieria: an ancient harbour submitted to two successive uplifts. International Journal of Nautical Archaeology 21(4), 317-327.

Evans, M.E. and Heller, F., 2003. Environmental magnetism: principles and applications of enviromagnetics. In: International Geophysics Series, vol. 86. Academic Press, 299 p.

Eyre, J. K., 1997. Frequency dependence of magnetic susceptibility for populations of single-domain grains. Geophysical Journal International 129, 209-211.

Fink, D., Hotchkis, M., Hua, Q., Jacobsen, G., Smith, A. M., Zoppi, U., Child, D., Mifsud, C., van der Gaast, H., Williams, A., Williams, M., 2004. The ANTARES AMS facility at ANSTO, NIM B 223-224, 109-115.

Finkler, C., Baika, K., Rigakou, D., Metallinou, G., Fischer, P., Hadler, H., Emde, K., Vött, A., 2017. Geoarchaeological investigations of a prominent quay wall in ancient Corcyra – implications for harbour development, palaeoenvironmental changes and tectonic geomorphology of Corfu island (Ionian Islands, Greece). Quaternary International. In press. Available online 16 May 2017.

Folk, R. L. and Ward, W. C, 1957. Brazos River bar, a study in the significance of grain size parameters. Journal of Sedimentary Petrology 27, 3.

Fortin, D., Francus, P., Gebhardt, C, Hahn, A., Kliem, P., Lisé-Pronovost, A., Roychowdhury, R., Labrie, J., St-Onge, G., 2013. Destructive and non-destructive density determination: method comparison and evaluation from the Laguna Potrok Aike sedimentary record, Quaternary Science Reviews 71, 147-153.

Galli, P. and Molin, D., 2014. Beyond the damage threshold: the historic earthquakes of Rome, Bulletin of Earthquake Engineering 12, 1277-1306.

Games, K. P., 1977. The magnitude of the paleomagnetic field: a new, non-thermal, non-detrital method using sun-dried bricks. Geophysical Journal of the Royal Astronomical Society 48, 315-329.

Games, K. P., 1983. Magnetisation of adobe bricks, In: Geomagnetism of baked clays and recent sediments, Eds. Creer, K. M., Tucholka, P., Barton, C. E., Elsevier, 324 p.

Gassend, J. M. *Le Navire Antique Du Lacydon*. Musée d'Histoire de Marseille, 1982.

Gilli, A., Anselmetti, F. S., Glur, L., Wirth, S. B., 2013. Lake sediments as archives of recurrence rates and intensities of past flood events, In: Dating Torrential Processes on Fans and Cones vol. 47, series Advances in Global Research, Eds. Schneuwly-Bollschweiler, M., Stoffel, M., Rudolf-Miklau, F., Springer, 423 p.

Giraudi C., Tata C., Paroli L., 2009. Late Holocene evolution of Tiber river delta and geoarchaeology of Claudius and Trajan Harbour, Rome. Geoarchaeology 24, 371-382.

Goiran, J.-P., Salomon, F., Mazzini, I., Bravard, J.-P., Pleuger, E., Vittori, C., Boetto, G., Christiansen, J., Arnaud, P., Pellegrino, A., Pepe, C., Sadori, L., 2014. Geoarchaeology confirms location of the ancient harbour basin of Ostia (Italy). Journal of Archaeological Science 41, 389–398.

Goiran, J.-P., Tronchère, H., Salomon, F., Carbonel, P., Djerbi, H., Ognard, C., 2010. Palaeoenvironmental reconstruction of the ancient harbours of Rome: Claudius and Trajan's marine harbours on the Tiber delta. Quaternary International 216(1–2), 3–13.

Goiran, J.-P., Tronchère, H., Collalelli, U., Salomon, F., Djerbi, H., 2009. Découverte d'un niveau marin biologique sur les quais de Portus: le port antique de Rome. Méditerranée 112 (1), 59-67.

Goiran, J.-P. and Morhange, C., 2001, Geoarcheology of ancient mediterranean harbours, Topoi 11 (2), 647-669.

Hadler, H., Vött, A., Fischer, P., Ludwig, S., Heinzelmann, M., Rohn, C., 2015. Temple-complex post-dates tsunami deposits found in the ancient harbour basin of Ostia (Rome, Italy). Journal of Archaeological Science 61: 78-89.

Herries, A.I.R., 2009. New approaches for integrating palaeomagnetic and mineral magnetic methods to answer archaeological and geological questions on Stone Age sites. In A. Fairbairn, S. O'Conner and B. Marwick (Eds), New Directions in Archaeological Science, pp.235–253. Terra Australis 28. Canberra: The Australian National University Press.

Heslop, D. and Dillon, M., 2007. Unmixing magnetic remanence curves without a priori knowledge, Geophysical Journal International 170 (2), 556-566.

Heslop, D., 2015. Numerical strategies for magnetic mineral unmixing. Earth-Science Reviews 150, 256-284.

Hounsfield, G.N., 1973. Computerized transverse axial scanning (tomography): I. description of system. British Journal of Radiology 46 (552), 1016-1022.

Keay S., Millett, M., Paroli, L., Strutt, K., 2005. Portus: an archaeological survey of the Portus of imperial Rome. Archaeological Monographs of the British School at Rome, 15, London.

Keay, S. and Paroli, L., 2011. Portus and its hinterland: recent archaeological research. Archaeological Monographs of the British School at Rome, 18, London.

Keller, G. and Pardo, A., 2004. Age and paleoenvironment of the Cenomanian–Turonian global stratotype section and point at Pueblo, Colorado. Marine Micropaleontology 51, 95-128.

King, J., and Channell J. E. T., 1991. Sedimentary magnetism, environmental magnetism, and magnetostratigraphy, in U.S. National Report to the International Union of Geodesy and Geophysics vol. 29, pp. 358–370, AGU, Washington, D. C.

Kondolf, G. M., Gao Y., Annandale, G.W., Morris, G.L., Jiang, E., Zhang, J., Cao, Y., Carling, P., Fu, K., Guo, Q., Hotchkiss, R., Peteuil, C., Sumi, T., Wang, H.-W., Wang, Z., Wei, Z., Wu, B., Wu, C., Yang, C.T., 2014. Sustainable sediment management in reservoirs and regulated rivers: Experiences from five continents, Earth's Future 2, 256-280.

Lisé-Pronovost, A., St-Onge, G., Gogorza, C., Haberzettl, T., Preda, M., Kliem, P., Francus, P. Zolitschka, B. and the PASADO science team, 2013. High-resolution paleomagnetic secular variation and relative paleointensity since the Late Pleistocene in Southern South America. Quaternary Science Reviews 71, 91-108.

Lie, S., Li, S., Shan, X., Gong, C., Yu, X., 2017. Classification, formation, and transport mechanisms of mud clasts. International Geology Review 59 (12), 1609-1620.

Liu, Q., Roberts, A.P., Larrasoaña, J.C., Banerjee, S.K., Guyodo, Y., Tauxe, L., Oldfield, F., 2012. Environmental magnetism: Principles and applications. Reviews of Geophysics 50, RG4002

Lurcock, P. C. and Wilson, G. S., 2012. PuffinPlot: A versatile, user-friendly program for paleomagnetic analysis, Geochemistry, Geophysics, Geosystems, 13, Q06Z45,

Maher, B.A., 1988. Magnetic properties of some synthetic sub-micron magnetites. Geophysical Journal Royal Astronomical Society 94, 83-96.

Marriner N., and Morhange, C., 2006. Geoarchaeological evidence for dredging in Tyre's ancient harbour, Levant. Quaternary Research 65, 64–171.

Marriner, N. and Morhange, C., 2007. Geoscience of ancient Mediterranean harbours, Earth Science Reviews 80, 137-194.

Marriner, N., Morhange, C., Doumet-Serhal, C., 2006. Geoarchaeology of Sidon's ancient harbours, Phoenicia. Journal of Archaeological Science 33, 1514–1535.

Marriner, N., Kaniewski, D., Morhange, C., Flaux, C., Giaime, M., Vacchi, M., Goff, J., 2017. Tsunamis in the Geological Record: Making Waves with a Cautionary Tale from the Mediterranean. Science Advances 3 (10).

McCann, A.M., 1979. The Harbour and Fishery Remains at Cosa, Italy. Journal of Field Archaeology 6 (4), 391-411.

McCormick, M., Büntgen, U., Cane, M. A., Cook, E. R., Harper, K., Huybers, P., Litt, T., Manning, S. W., Mayewski, P. A., More, A. F. M., Nicolussi, K., Tegel, W., 2012. Climate Change during and after the Roman Empire: Reconstructing the Past from Scientific and Historical Evidence, Journal of Interdisciplinary History 43 (2), 169-220.

Mensing, S.A., Tunno, I., Sagnotti, L., Florindo, F., Noble, P., Archer, C., Zimmerman, S., Pavon-Carrasco, F.J, Cifani, G., Passigli, S., Piovesan, G., 2015. 2700 years of Mediterranean environmental change in central Italy: a synthesis of sedimentary and cultural records to interpret past impacts of climate on society. Quaternary Science Reviews 116, 72-94.

Millet, B., Tronchère, H., Goiran, J.-P., 2014. Hydrodynamic modeling of the roman harbour of Portus in the Tiber delta: the impact of the north-eastern channel on current and sediment dynamics. Geoarchaeology 29, 357-370.

Montero-Serrano, J.C., Bout-Roumazeilles, V., Tribovillard, N., Sionneau, T., Riboulleau, A., Bory, A., Flower, B., 2009. Sedimentary evidence of deglacial megafloods in the northern Gulf of Mexico (Pigmy Basin). Quaternary Science Reviews 28, 3333–3347.

Montero-Serrano, J.C., Foellmi, K.B., Adatte, T., Spangenberg, J.E., Tribovillard, N., Fantasia, A., Suan, G., 2015. Continental weathering and redox conditions during the early Toarcian Oceanic Anoxic Event in the northwestern Tethys: Insight from the Posidonia Shale section in the Swiss Jura Mountains. Palaeogeography Palaeoclimatology Palaeoecology 429, 83–99.

Moore, F.G., 1950. Three Canal Projects, Roman and Byzantine. American Journal of Archaeology 54(2), 97-111.

Morhange, C., and Marriner, N., 2010. Paleo-Hazards in the Coastal Mediterranean: A Geoarchaeological Approach. In Martini, I.P, and Chesworth, W. (Eds.), Landscapes and Societies, Springer, 478 p.

Morhange, C., Blanc, F., Schmitt-Mercury, S., Bourcier, M., Carbonel, P., Oberlin, C, Prone, A., Vivent, D., Hesnard, A., 2003. Stratigraphy of late Holocene deposits of the ancient harbour of Marseille, southern France. The Holocene 13 (4), 593–604.

Mort, H.P., Adatte, T., Keller, G., Bartels, D., Föllmi, K.B., Steinmann, P., Berner, Z., Chellai, E.H., 2008. Organic carbon deposition and phosphorus accumulation during oceanic anoxic event 2 in Tarfaya, Morocco. Cretaceous Research 29, 1008-1023.

Mulder, T., Syvitski, J.P.M., Migeon, S., Faugères, J.-C., Savoye, B., 2003. Marine hyperpycnal flows: initiation, behavior and related deposits. A review. Marine Petroleum Geology 20, 861–882.

Mulder, T., Zaragosi, S., Jouanneau, J.-M., Bellaiche, G., Guérinaud, S., Querneau, J., 2009. Deposits related to the failure of the Malpasset Dam in 1959, an analogue for hyperpycnal deposit from jökulhlaups. Marine Geology 260, 81-89.

Mulder, T., and Chapron, E., 2011, Flood deposits in continental and marine environments: Character and significance, In R. M. Slatt and C. Zavala, Eds., Sediment transfer from shelf to deep water—Revisiting the delivery system: AAPG Studies in Geology 61, p. 1–30.

Paroli, L., 2005. The Basilica Portuense. In Portus: An Archaeological Survey of the Port of Imperial Rome, edited by S. Keay, M. Millett, L. Paroli, and K. Strutt, 258–68. Archaeological Monographs of the British School at Rome 15. London.

Passega, R., 1964. Grain size representation by CM patterns as a geological tool. Journal of Sedimentary Petrology 34, 830–847.

Petschick, R., 2000. MacDiff 4.2 Manual. MacDiff [Online]. Available from World Wide Web:http://www.geologie.unifrankfurt.de/Staff/Homepages/Petschick/Classicsoftware.html#MacDiff.

Pliny. Natural History, Volume III: Books 8-11. Translated by H. Rackham. Loeb Classical Library 353. Cambridge, MA: Harvard University Press, 1940

Pomey, P., 1995. Les épaves grecques et romaines de la place Jules Verne à Marseille. Compte-Rendus Académie Inscriptions et Belles Lettres, avril-juin, 459–484.

Pomey, P., and E. Rieth. *L'archéologie Navale*. Collection "Archéologiques." Paris: Editions Errance, 2005.

Pomey, P., and A. Tchernia. "Le Tonnage Maximum Des Navires de Commerce Romains." *Archeonautica*, no. 2 (1978): 233–51.

Reimer P.J., Bard E., Bayliss A., Beck J.W., Blackwell P.G., Bronk Ramsey C., Buck C.E., Cheng H., Edwards R.L., Friedrich M., Grootes P.M., Guilderson T.P., Haflidason H., Hajdas I., Hatté C., Heaton T.J., Hogg A.G., Hughen K.A., Kaiser K.F., Kromer B., Manning S.W., Niu M., Reimer R.W., Richards D.A., Scott E.M., Southon J.R., Turney C.S.M., van der Plicht, 2013. IntCal13 and MARINE13 radiocarbon age calibration curves 0-50000 years calBP, Radiocarbon 55(4).

Röbke, B.R., Vött, A. (2017): The tsunami phenomenon. Progress in Oceanography 159: 296-322.

Roberts, A. P., 2015. Magnetic mineral diagenesis, Earth Science Reviews 151, 1-47.

Roberts, A. P., Pike, C.R., Verosub, K.L., 2000. First-order reversal curve diagrams: a new tool for characterizing the magnetic properties of natural samples. Journal of Geophysical Research 105 (B12), 28461-28475.

Sadler, P.M., 1981. Sediment accumulation rates and the completeness of stratigraphic sections, The Journal of Geology 89 (5), 569-584.

Sadori, L., Giardini, M., Giraudi, C., Mazzini, I., 2010. The plant landscape of the imperial harbour of Rome. Journal of Archaeological Science 37, 3294–3305.

Salomon, F., Delile, H., Goiran, J.-P., Bravard, J.-P., Keay, S., 2012. The Canale Di Comunicazione Traverso in Portus: the Roman sea harbour under river influence (Tiber Delta, Italy). Géomorphologie 1, 75–90.

Salomon, F., Goiran, J.-P., Bravard, J.-P., Arnaud, P., Djerbi, H., Kay, S., Keay, S., 2014. A harbour-canal at Portus: a geoarchaeological approach to the Canale Romano: Tiber delta, Italy. Water History 6, 31-49.

Salomon, F., Keay, S., Carayon, N., Goiran, J.-P., 2016. The Development and Characteristics of Ancient Harbours—Applying the PADM Chart to the Case Studies of Ostia and Portus. PLOS ONE 11(9) 0162587.

St-Onge, G., Mulder, T., Piper, D.J.W., Hillaire-Marcel, C. and Stoner, J.S. 2004. Earthquake and flood-induced turbidites in the Saguenay Fjord (Québec): a Holocene paleoseismicity record. Quaternary Science Reviews 23, 283-294.

St-Onge, G., Mulder, T., Francus, P., Long., B. 2007. Continuous physical properties of cored marine sediments. In : C. Hillaire-Marcel et A. de Vernal (Eds.), Proxies in Late Cenozoic Paleoceanography, Elsevier, pp. 63-98.

Stober, J. C., and Thompson, R., 1979. An investigation into the source of magnetic minerals in some Finnish lake sediments, Earth and Planetary Science Letters 45, 464–474.

Stock, F., Knipping, M., Pint, A. Pint, Ladstatter, S., Delile, H., Heiss, A.G., Laermanns, H., Mitchell, P.D., Ployer, R., Steskal, M., Thanheiser, U., Urz, R., Wennrich, V., Bruckner, H., 2016. Human impact on Holocene sediment dynamics in the Eastern Mediterranean - the example of the Roman harbour of Ephesus. Earth Surface Processes and Landforms 41, 980-996.

Storen, E. N., Dahl, S. O., Nesje, A., Paasche, O., 2010. Identifying the sedimentary imprint of high-frequency Holocene river floods in lake sediments: development and application of a new method. Quaternary Science Reviews 29, 3021-3033.

Stuiver, M., Reimer, P.J., Reimer, R.W., 2017, CALIB 7.1 [WWW program] at http://calib.org

Syme, R., 1985. The dating of Pliny's latest letters, The Classical Quarterly (New Series) 35 (1), 176-185.

Tauxe, L., 1993. Sedimentary records of relative paleointensity of the geomagnetic field: theory and practice. Reviews of Geophysics 31 (3), 319-354.

Testaguzza, O., 1970. Portus: illustrazione dei porti di Claudio e Traiano. Julia Editrice, Rome.

Vött, A., Hadler, H., Willershäuser, T., Ntageretzis, K., Brückner, H., Warnecke, H., Grootes, P.M., Lang, F., Nelle, O., Sakellariou, D., 2014. Ancient harbours used as tsunami sediment traps – the case study of Krane (Cefalonia Island, Greece). In: Ladstätter, S., Pirson, F., Schmidts, T. (Hrsg.): Häfen und Hafenstädte im östlichen Mittelmeerraum von der Antike bis in byzantinische Zeit. Neue Entdeckungen und aktuelle Forschungsansätze. Harbors and harbor cities in the eastern Mediterranean from Antiquity to the Byzantine Period: Recent discoveries and current approaches. Byzas 19, Veröffentlichungen des Deutschen Archäologischen Instituts Istanbul, Österreichisches Archäologisches Institut Sonderschriften 52, Vol. II, S. 743-771. Istanbul.

Vuorinen, H.S., 1997. Diseases in the ancient world, Hippokrates (Helsinki), 74-97.

Weeks, R., Laj, C., Endigoux, L., Fuller, M., Roberts, A., Manganne, R., Blanchard, E., Goree, W., 1993. Improvements in long-core measurements techniques: applications in paleomagnetism and paleoceanography. Geophysical Journal International 114, 651-662.

FIGURE CAPTIONS

Figure 1. A) Location of Portus near the Tiber River in Italy and B) position of the coring sites, including the stationary piston cores CPS1 and CPS4, and previous rotary cores discussed in the text. κ is magnetic susceptibility. C) Modern and D) ancient configuration of Portus (modified from Goiran et al., 2010). E) Piston coring of core CPS1 in September 2011.

Figure 2. The stratigraphy of core CPS1 is primarily based on A) CT number, B) gamma-ray attenuation, C) magnetic susceptibility, and D) mud content. Core CT-scan images and photographs are on the left, with the sampling log (cubes and u-channels) and simplified stratigraphic log with the types of deposit for units A to F. Square symbols are used for data measured on cube samples, and simple line for u-channel samples. The dashed line indicates the D1/D2 transition within the harbour deposit. E) Typical grain size distributions for each deposit type.

Figure 3. Bulk, clay, and magnetic mineralogy results. A simplified stratigraphic log with deposit type is shown on the left. The dashed line indicates the D1/D2 transition within the harbour deposit.

Figure 4. Magnetic end-member (EM) analysis with three components representing distinct magnetic particle populations in core CPS1 obtained by unmixing 50 isothermal remanent magnetization (IRM) acquisition curves (Heslop and Dillon, 2007; Heslop, 2015). A) IRM end-members and B) down-core variations of the relative proportions of EM1, 2, and 3. Magnetic properties and multi-proxy investigations indicate that EM1 represents detrital minerals of fluvial origin, EM2 represents biogenic minerals from the harbour, and EM3 represents lower coercivity multi-domain (MD) particles.

Figure 5. Magnetic grain size indicators. A) Coercivity ratio H_{cr}/H_c, B) magnetization ratio M_r/M_s, C) median destructive field of the anhysteretic remanent magnetization MDF_{ARM}, and D) frequency-dependent magnetic susceptibility $\chi_{FD\%}$, compared with bulk grain size indicators E) mud content, and F) D90 vs D50 biplot (Passega, 1964) for core CPS1.

Figure 6. Radiocarbon-based chronology for core CPS1. Bayesian age modelling of A) full CPS1 core in a Palaeoenvironmental Age-Depth Model (PADM) chart (Salomon et al., 2016) and B) the harbour deposit. Light grey distributions are calibrated ages and dark grey are modelled ages with a simple sequence Bayesian model performed with the Charcoal Outlier Model using OxCal v4.2.3 (Bronk Ramsey and Lee, 2013). A simplified stratigraphic log and lithology for units A to F are shown.

Figure 7. Comparison of Portus core stratigraphy and magnetic susceptibility data along a NNW-SSE transect. The cores are aligned at the proposed chronostratigraphic marker at the time of decommissioning Canale Traverso. Debris dammed Canale Traverso at the access channel entrance (core CPS1; this study) and resulted in more marine conditions in the access channel (core TR14; Delile et al., 2014) and more fluvial conditions upstream in Canale Traverso (core CT1; Salomon et al., 2012). The top of core TR14 is at -0.19 m relative to current sea level, core CPS1 at +0.3 m, and CT1 at +1.8 m. See core locations in Figure 1.

Figure 8. Core CPS1 reconstructed depositional history.

Figure 9. Typical demagnetization plots, orthogonal projection diagrams, and stereonet projections for A-B) the harbour deposit, C) the hyperpycnal deposit, and D) the dredged deposit. Demagnetization steps considered for the principal component analysis (PCA) calculation are indicated and highlighted in red. Stable and well defined paleomagnetic directions were obtained for (A, B) harbour mud samples and most reworked deposits, with inclination values (bold) near the expected GAD field value of 60.8° (D). In contrast, flattened to reversed polarity inclinations are obtained within the high-energy flow (C).

Figure 10. Magnetic parameters for identified reworked deposits in core CPS1. Magnetic susceptibility (κ), saturation magnetization (M_s), hard isothermal remanent magnetization (HIRM), paleomagnetic inclination, the magnetic grain size indicator κ_{ARM}/κ_{LF}, and concentration of magnetic population EM1 are proxies for the hyperpycnal deposit, with peak values in the central debris layer. Grain size data indicate a typical hyperpycnite sequence, coarsening upward from predominantly fine silts to coarse sands during the waxing flow, and fining upward to fine sands during the waning flow. The dredged deposit has relatively homogenous properties within the sand, with distinct values associated with mud clasts. Note that inclination values near the geocentric axial dipole (GAD) value are recorded in the muddy sands of the dredged deposit.

SUPPLEMENTARY FIGURES

Sup. Figure 1. Results of rock- and paleo-magnetic pilot studies.

Sup. Figure 2. First-order reversal curve (FORC) diagrams and hysteresis loops for samples from sub-units D1 and D2 of core CPS1.

TABLES

Table 1. Laboratory analyses performed on core CPS1.

Table 2. Radiocarbon dating of core CPS1, calibration, and age modelling.

Table 3. Summary of data and hypotheses for the event deposits of core CPS1

Table 1. Laboratory analyses performed on core CPS1.

Analysis	Resolution
CT scan (density proxy)	0.06 cm
Gamma ray attenuation (density proxy)	1 cm
Volumetric magnetic susceptibility (κ)	1 cm
Image scan	0.025 cm
Volumetric magnetic susceptibility (κ)	0.5 cm
Natural remanent magnetisation (NRM)	1 cm
Anhysteretic remanent magnetisation (ARM)	1 cm
Frequency dependant magnetic susceptibility (χ_{FD})	10 cm
Laser granulometry (bulk grain size)	10 cm
X-ray diffraction (bulk mineralogy)	10 cm
Hysteresis curves and properties (M_r, M_s, H_{cr}, H_c)	10 cm
Isothermal remanent magnetisation (IRM) acquisition	10 cm
First-order reversal curves (FORC)	7 samples

Table 1. Radiocarbon dating of core CPS1, calibration, and age modelling.

Core depth		Sample name	Laboratory	Material	$\delta^{13}C$	^{14}C age	Calibrated age (AD/BC)		Modelled age (AD/BC)		
(cm)	Unit		code			(yr BP)	min	max	min	max	median
170-171	D	CPS1-3/25-26cm	OZS602	pollen/charcoal	-25.0 ± 0.1	1925 ± 20	AD 28	AD 127	AD 163	AD 616	AD 294
227-228	D	CPS1-3/82-83cm	OZS601	coniferous bud	-24.5 ± 0.1	1810 ± 25	AD 131	AD 311	AD 155	AD 311	AD 220
269-270	D	CPS1-4/25-26cm	OZS600	seed	-23.8 ± 0.1	1865 ± 25	AD 80	AD 225	AD 140	AD 226	AD 186
357-358	D	CPS1-5/15-16cm	OZS599	seed	-25.3 ± 0.1	1810 ± 20	AD 131	AD 310	AD 128	AD 202	AD 155
414-415	C	CPS1-5/72-73cm	OZS598	pollen/charcoal	-25.0 ± 0.1	2650 ± 20	833 BC	795 BC	735 BC	AD 55	432 BC
580-581	A	CPS1-7/46-47cm	OZS597	seed	-26.2 ± 0.1	2470 ± 25	765 BC	492 BC	764 BC	434 BC	625 BC

Table 3. Summary of data and hypotheses for the event deposits of core CPS1.

		Climate-driven		Human-driven	
		Tsunami	Flood	Canal gate	Dredging
		HIGH ENERGY FLOW			LOW ENERGY FLOW
Unit C	Fining upward	■	■	■	■
	Debris layer (30 cm)	■		■	
	Fluvial signature of debris layer		■	■	
	Coarsening upward	■	■	■	
Unit B	GAD paleomagnetic inclination				■
	Angular mud clasts				■
	Massive (ungraded) sands				■
	Erosive contact	■	■	■	■

ACCEPTED MANUSCRIPT

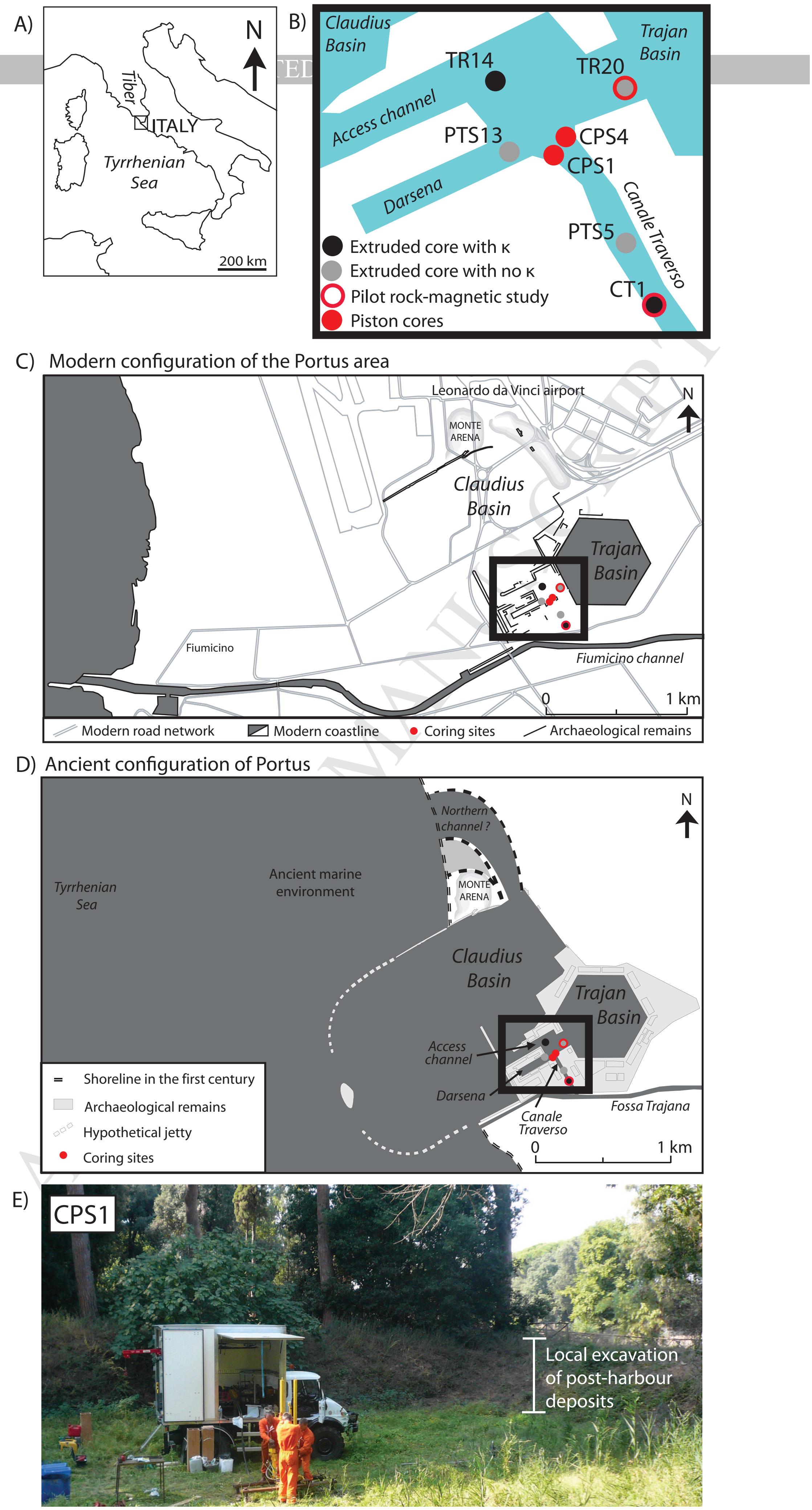
A)
N
Tiber
ITALY
Tyrrhenian Sea
200 km
B)
Claudius Basin
Trajan Basin
TR14
TR20
Access channel
PTS13
CPS4
CPS1
Darsena
Canale Traverso
PTS5
CT1
Extruded core with κ
Extruded core with no κ
Pilot rock-magnetic study
Piston cores
C) Modern configuration of the Portus area
Leonardo da Vinci airport
N
MONTE ARENA
Claudius Basin
Trajan Basin
Fiumicino
Fiumicino channel
0
1 km
Modern road network
Modern coastline
Coring sites
Archaeological remains
D) Ancient configuration of Portus
N
Northern channel ?
Tyrrhenian Sea
Ancient marine environment
MONTE ARENA
Claudius Basin
Trajan Basin
Access channel
Darsena
Canale Traverso
Fossa Trajana
0
1 km
Shoreline in the first century
Archaeological remains
Hypothetical jetty
Coring sites
E)
CPS1
Local excavation of post-harbour deposits

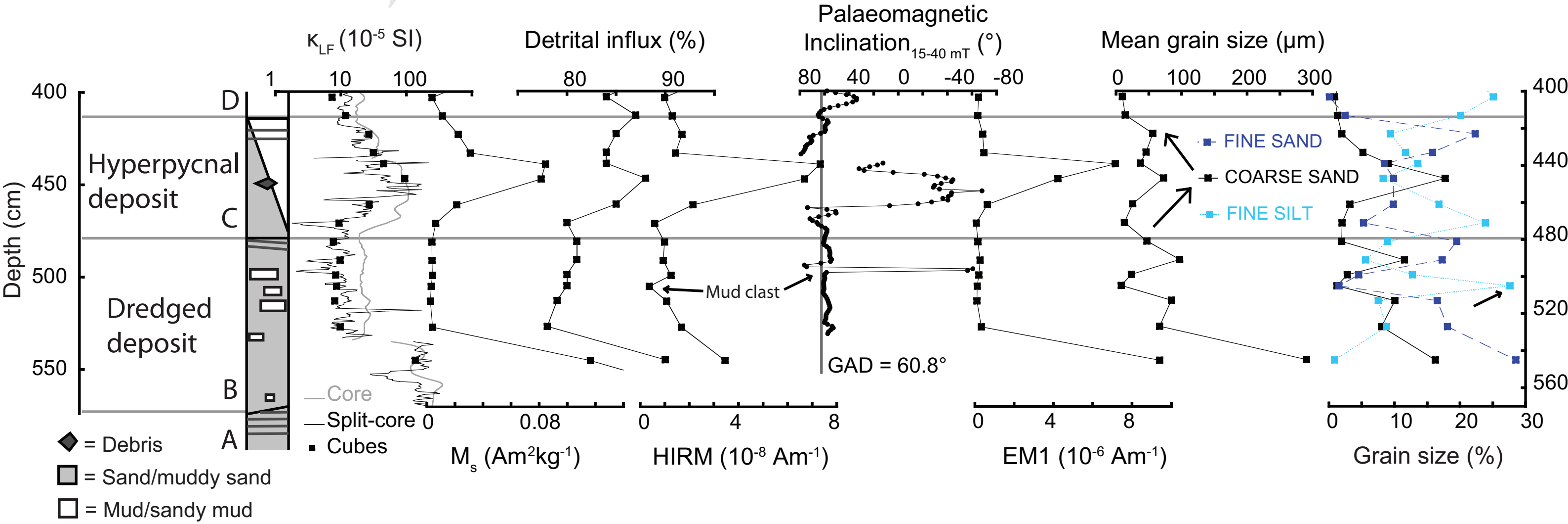

Depth (cm)
400
450
500
550
D
C
B
A
Hyperpycnal deposit
Dredged deposit
κLF (10-5 SI)
1
10
100
Core
Split-core
Cubes
Ms (Am2kg-1)
0
0.08
Detrital influx (%)
80
90
HIRM (10-8 Am-1)
0
4
8
Mud clast
Palaeomagnetic Inclination15-40 mT (°)
80
40
0
-40
-80
GAD = 60.8°
EM1 (10-6 Am-1)
0
4
8
Mean grain size (μm)
0
100
200
300
FINE SAND
COARSE SAND
FINE SILT
Grain size (%)
0
10
20
30
400
440
480
520
560
= Debris
= Sand/muddy sand
= Mud/sandy mud

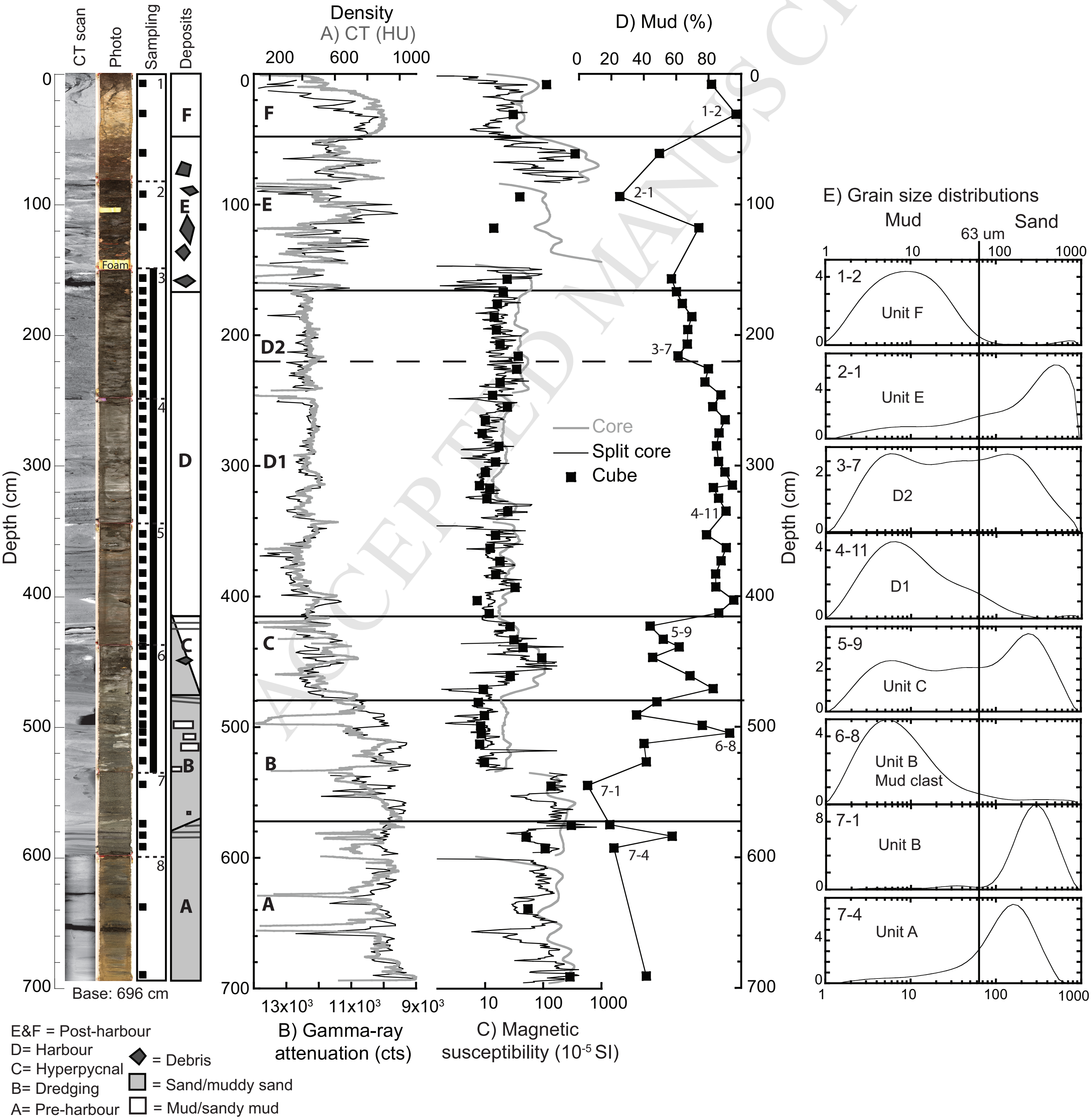

CT scan
Photo
Sampling
Deposits
Depth (cm)
Base: 696 cm
Density
A) CT (HU)
B) Gamma-ray attenuation (cts)
C) Magnetic susceptibility (10-5 SI)
D) Mud (%)
Core
Split core
Cube
Foam
E) Grain size distributions
Mud
Sand
63 um
Unit F
Unit E
D2
D1
Unit C
Unit B Mud clast
Unit B
Unit A
E&F = Post-harbour
D= Harbour
C= Hyperpycnal
B= Dredging
A= Pre-harbour
= Debris
= Sand/muddy sand
= Mud/sandy mud

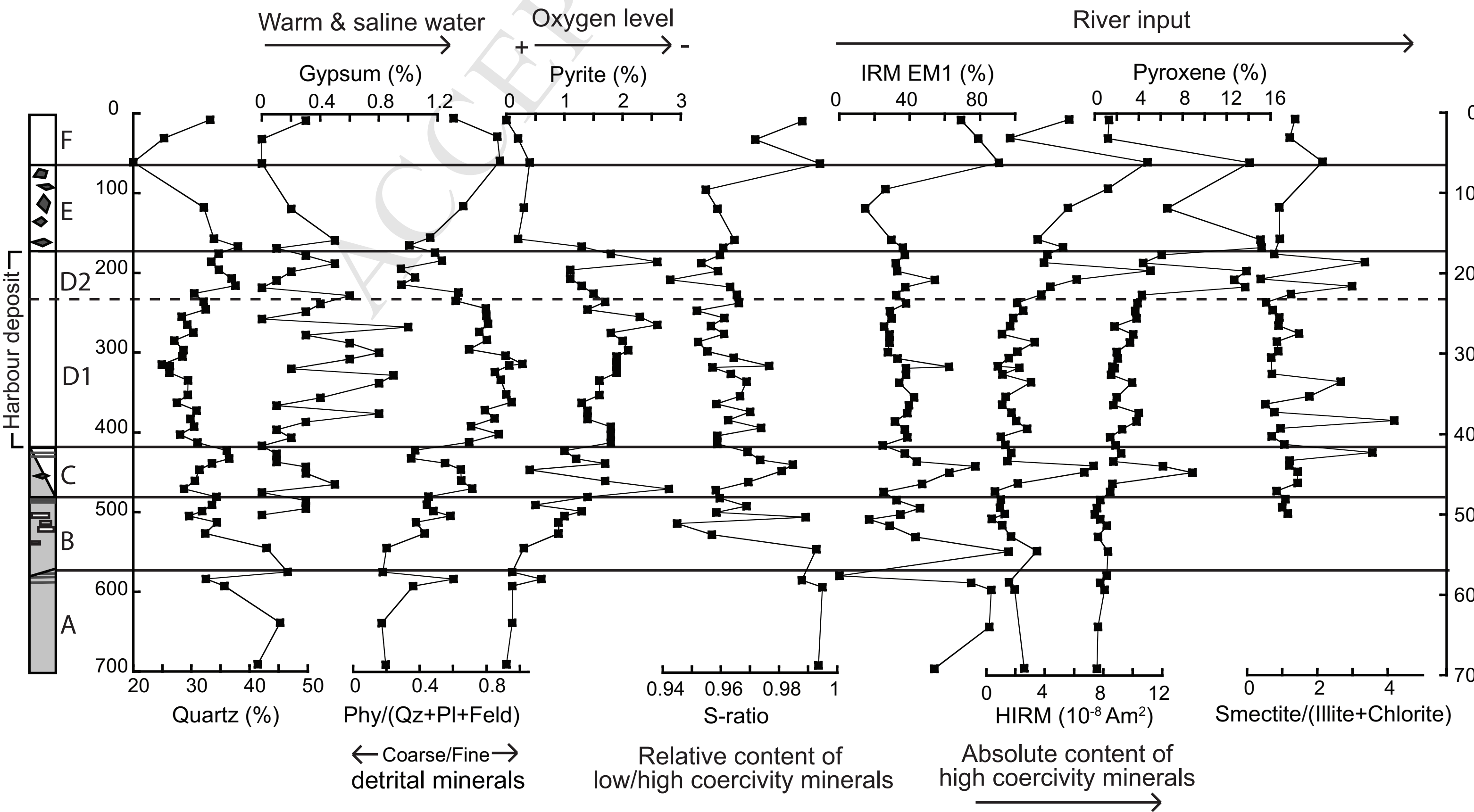
Warm & saline water
Oxygen level
+
-
River input
Gypsum (%)
0 0.4 0.8 1.2
Pyrite (%)
0 1 2 3
IRM EM1 (%)
0 40 80
Pyroxene (%)
0 4 8 12 16
0 100 200 300 400 500 600 700
F
E
D2
D1
C
B
A
Harbour deposit
20 30 40 50
Quartz (%)
0 0.4 0.8
Phy/(Qz+Pl+Feld)
0.94 0.96 0.98 1
S-ratio
0 4 8 12
HIRM (10^{-8} Am^2)
0 2 4
Smectite/(Illite+Chlorite)
Coarse/Fine
detrital minerals
Relative content of
low/high coercivity minerals
Absolute content of
high coercivity minerals

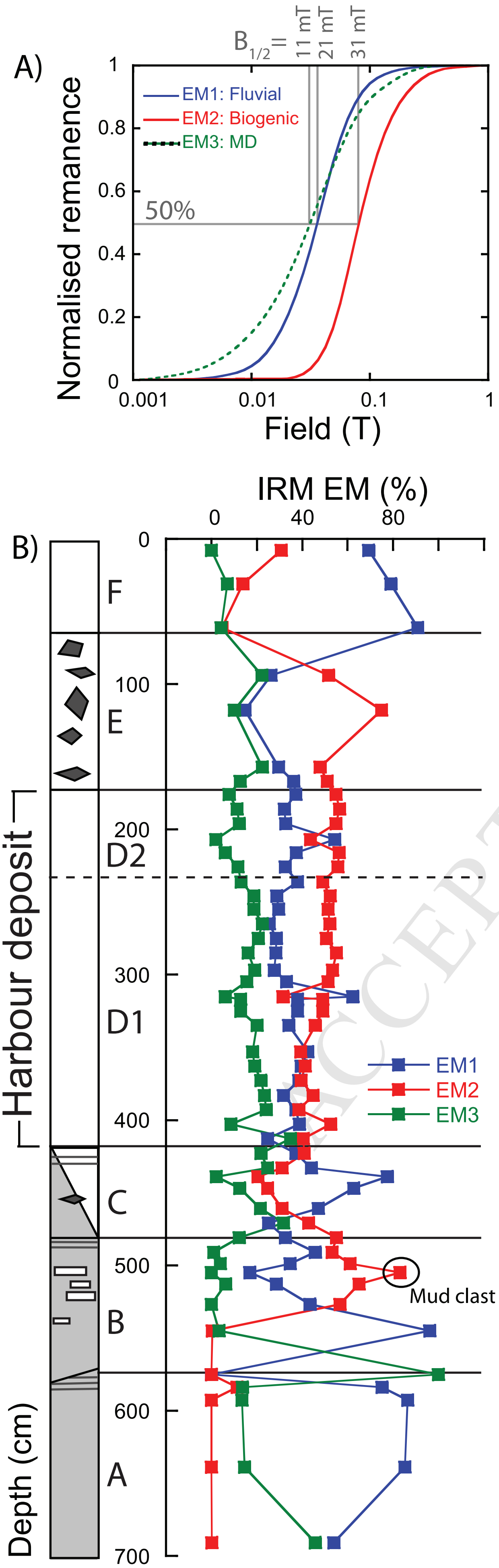

A)
B1/2=
11 mT
21 mT
31 mT
EM1: Fluvial
EM2: Biogenic
EM3: MD
50%
Normalised remanence
Field (T)
B)
IRM EM (%)
F
E
D2
D1
C
B
A
EM1
EM2
EM3
Mud clast
Harbour deposit
Depth (cm)

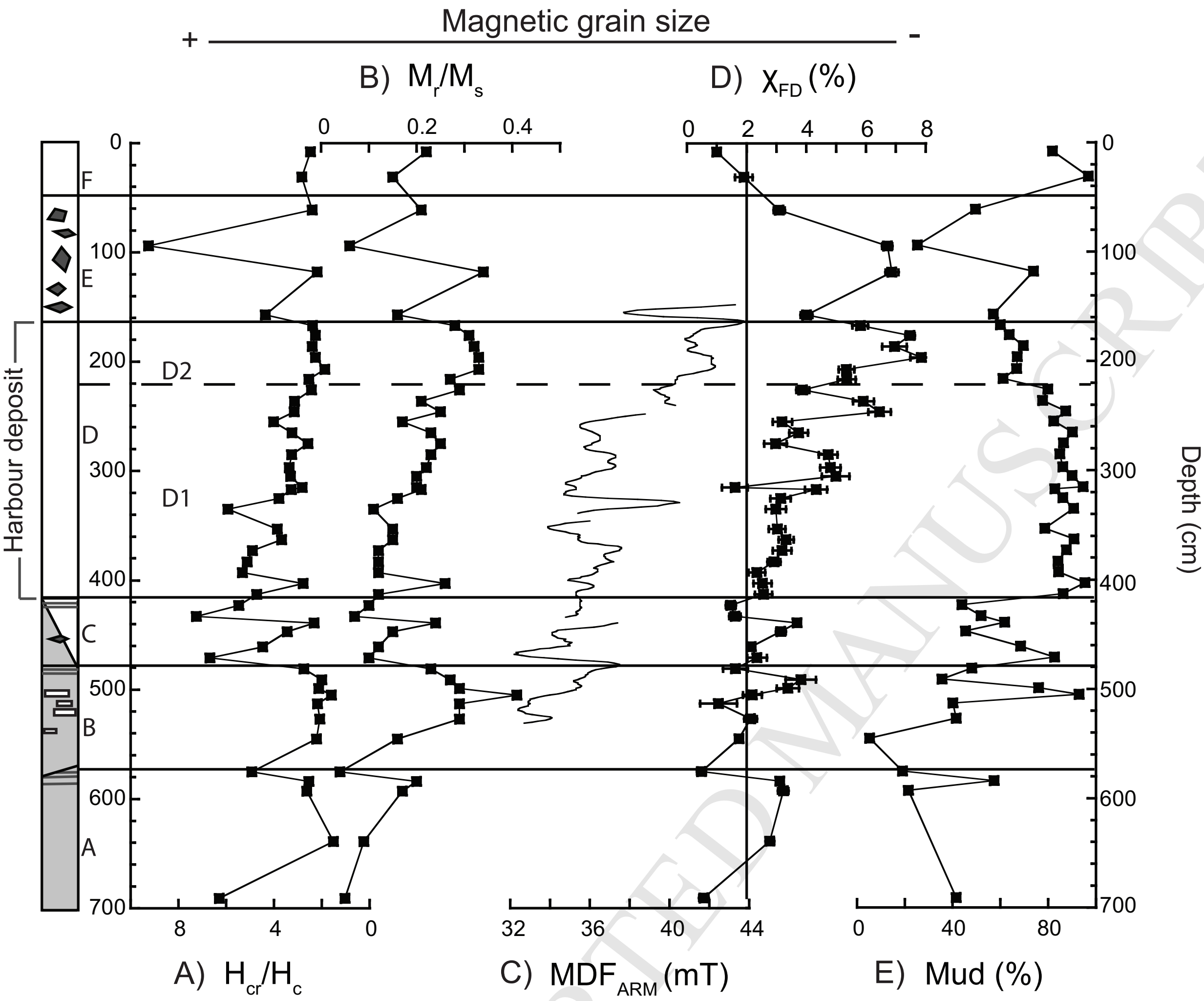

Magnetic grain size
+
-
B) M_r/M_s
D) χ_{FD} (%)
A) H_{cr}/H_c
C) MDF_{ARM} (mT)
E) Mud (%)
Depth (cm)
Harbour deposit
F
E
D2
D
D1
C
B
A

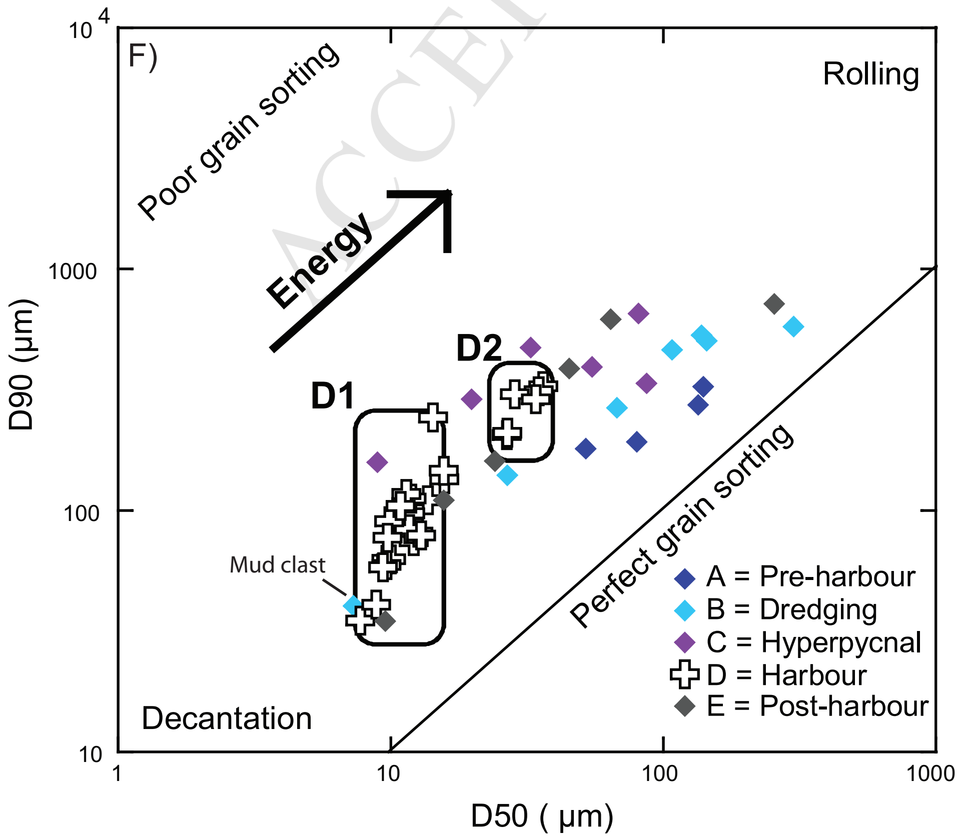

F)
Poor grain sorting
Rolling
Energy
D2
D1
Mud clast
Perfect grain sorting
Decantation
A = Pre-harbour
B = Dredging
C = Hyperpycnal
D = Harbour
E = Post-harbour
D90 (µm)
D50 (µm)

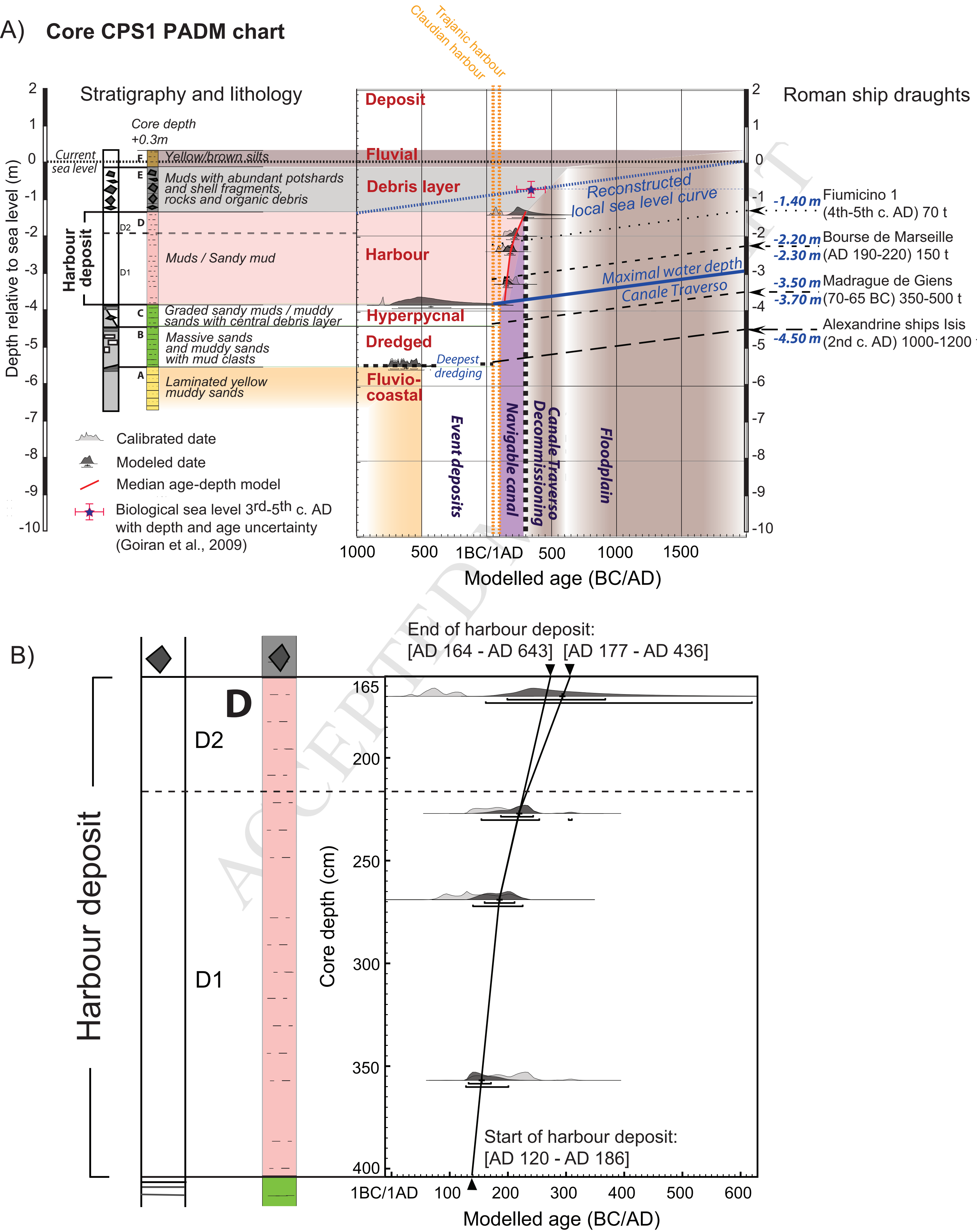

A) Core CPS1 PADM chart
Stratigraphy and lithology
Roman ship draughts
Core depth +0.3m
Current sea level
Yellow/brown silts
Muds with abundant potshards and shell fragments, rocks and organic debris
Muds / Sandy mud
Graded sandy muds / muddy sands with central debris layer
Massive sands and muddy sands with mud clasts
Laminated yellow muddy sands
Harbour deposit
Depth relative to sea level (m)
Trajanic harbour
Claudian harbour
Deposit
Fluvial
Debris layer
Harbour
Hyperpycnal
Dredged
Fluvio-coastal
Deepest dredging
Reconstructed local sea level curve
Maximal water depth Canale Traverso
Event deposits
Navigable canal
Decommissioning
Canale Traverso
Floodplain
-1.40 m Fiumicino 1 (4th-5th c. AD) 70 t
-2.20 m -2.30 m Bourse de Marseille (AD 190-220) 150 t
-3.50 m -3.70 m Madrague de Giens (70-65 BC) 350-500 t
-4.50 m Alexandrine ships Isis (2nd c. AD) 1000-1200
Calibrated date
Modeled date
Median age-depth model
Biological sea level 3rd-5th c. AD with depth and age uncertainty (Goiran et al., 2009)
Modelled age (BC/AD)
B)
End of harbour deposit: [AD 164 - AD 643] [AD 177 - AD 436]
D
D2
D1
Harbour deposit
Core depth (cm)
Start of harbour deposit: [AD 120 - AD 186]
Modelled age (BC/AD)

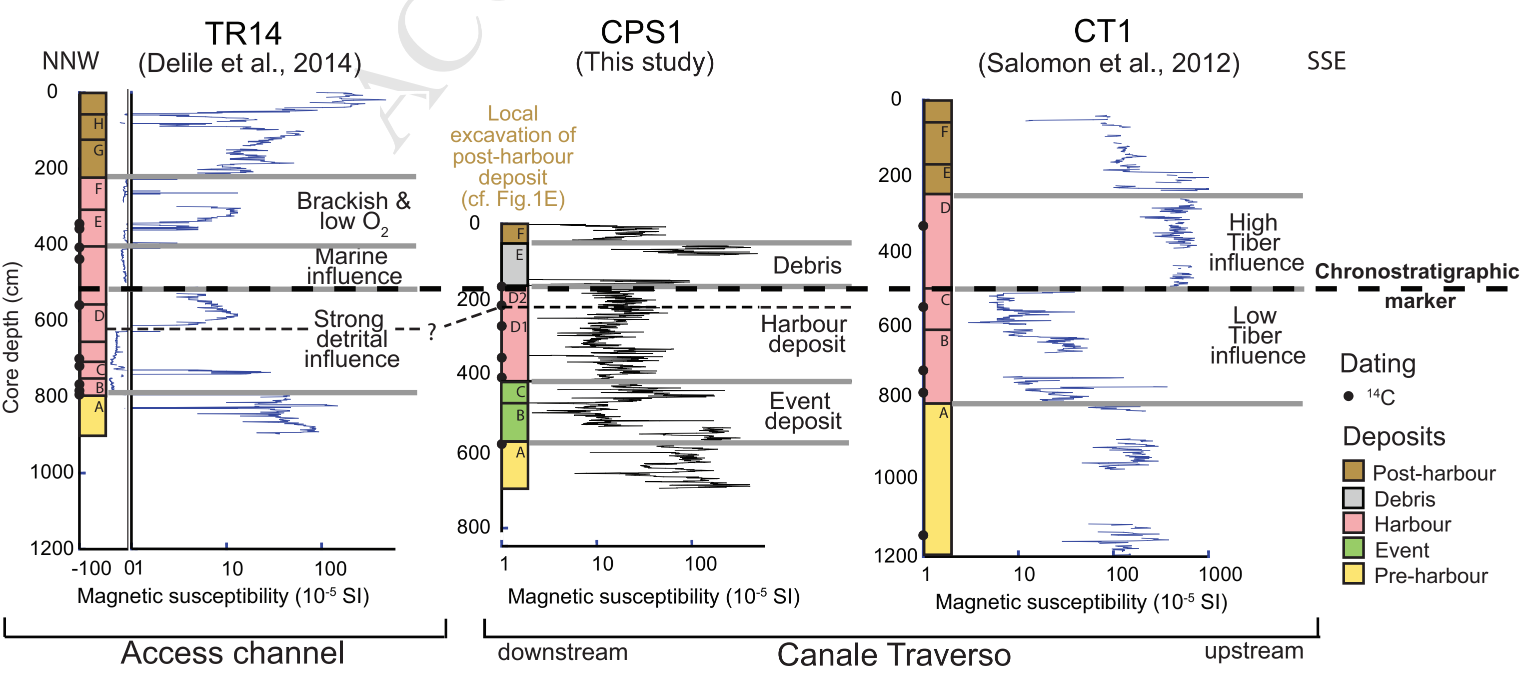

NNW
TR14
(Delile et al., 2014)
CPS1
(This study)
CT1
(Salomon et al., 2012)
SSE
Brackish & low O_2
Marine influence
Strong detrital influence
Local excavation of post-harbour deposit (cf. Fig.1E)
Debris
Harbour deposit
Event deposit
High Tiber influence
Low Tiber influence
Chronostratigraphic marker
Core depth (cm)
Magnetic susceptibility (10^{-5} SI)
Dating
^{14}C
Deposits
Post-harbour
Debris
Harbour
Event
Pre-harbour
Access channel
downstream
Canale Traverso
upstream

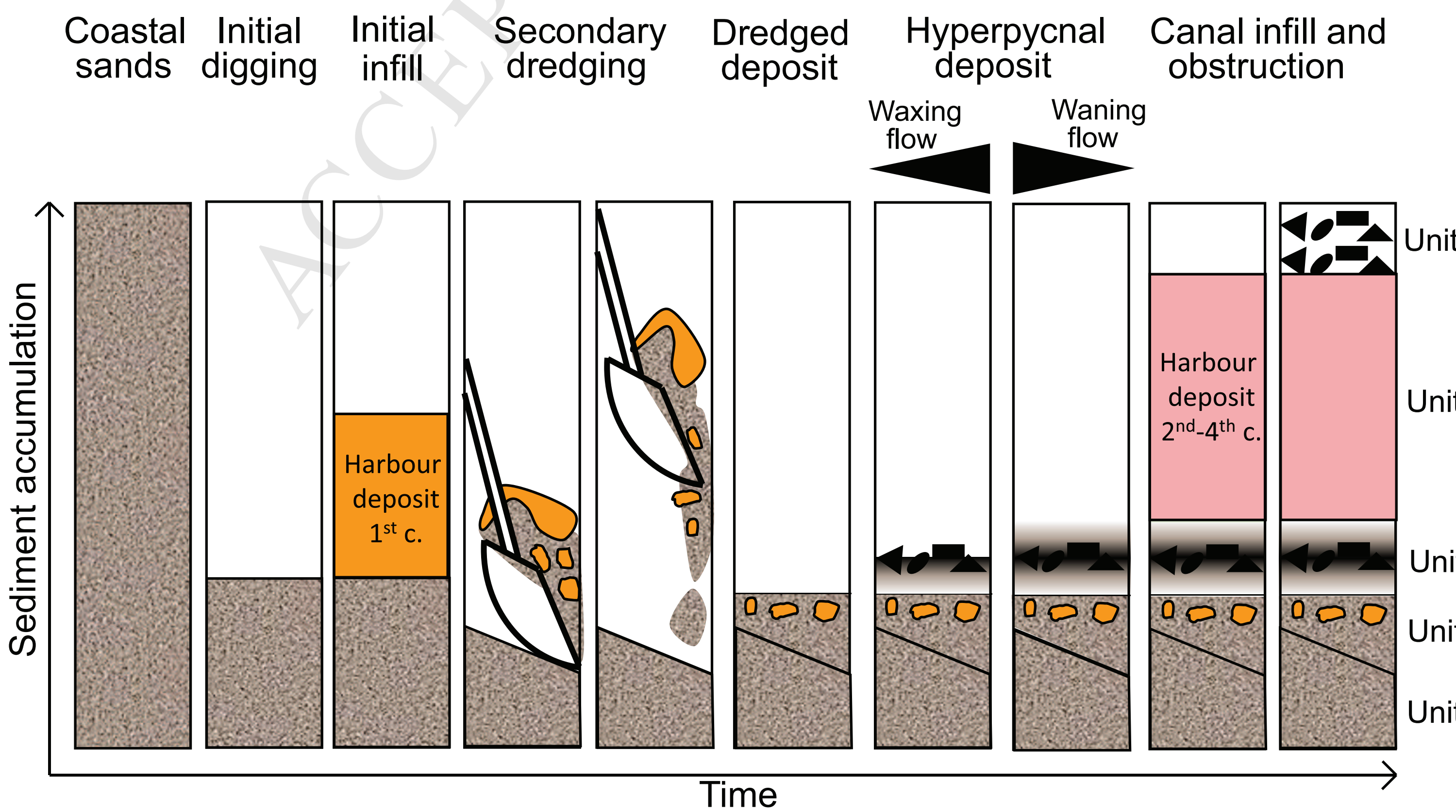

Coastal sands
Initial digging
Initial infill
Secondary dredging
Dredged deposit
Hyperpycnal deposit
Waxing flow
Waning flow
Canal infill and obstruction
Harbour deposit 1st c.
Harbour deposit 2nd-4th c.
Sediment accumulation
Time

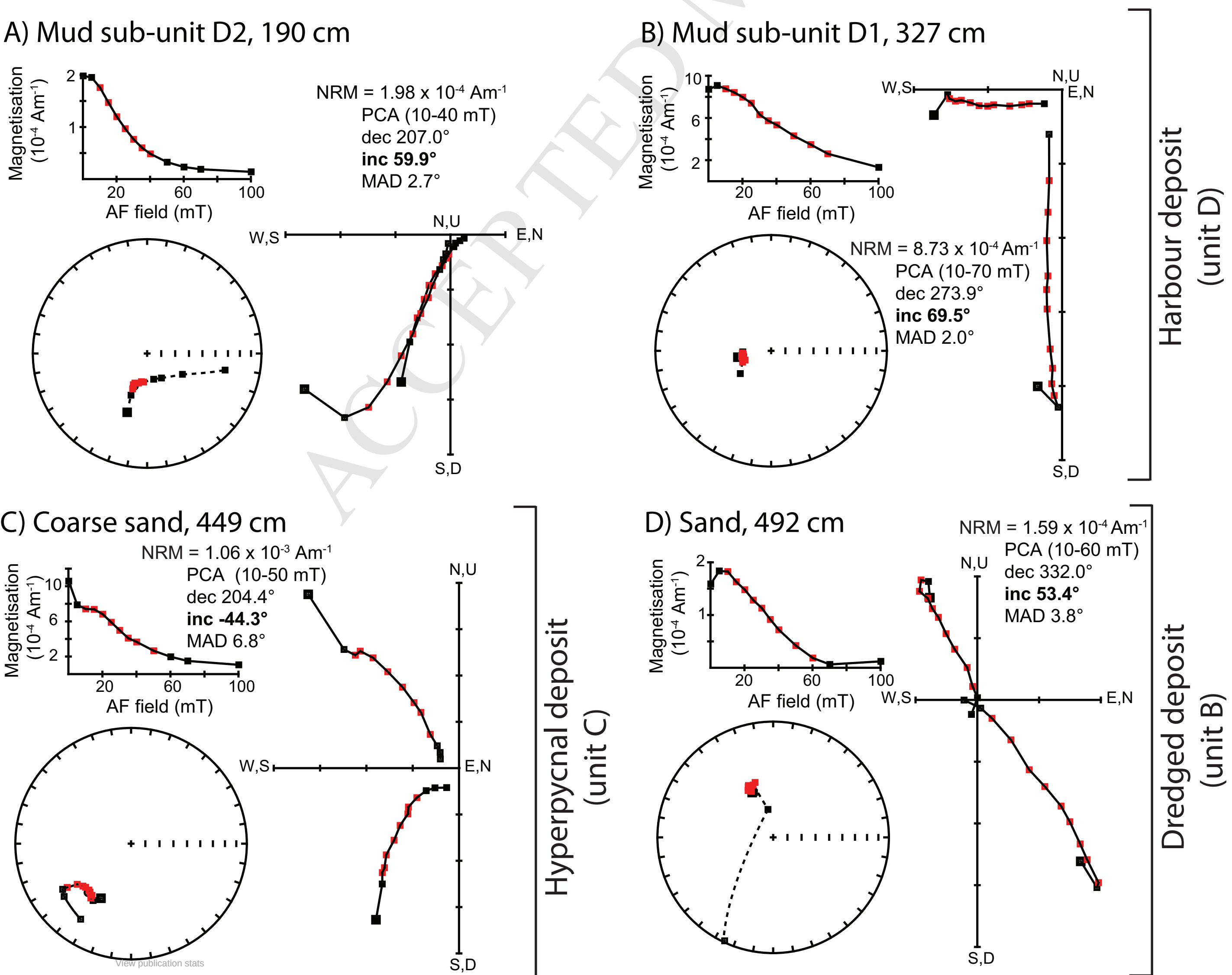
A) Mud sub-unit D2, 190 cm
Magnetisation (10-4 Am-1)
AF field (mT)
NRM = 1.98 x 10-4 Am-1
PCA (10-40 mT)
dec 207.0°
inc 59.9°
MAD 2.7°
W,S
N,U
E,N
S,D
B) Mud sub-unit D1, 327 cm
Magnetisation (10-4 Am-1)
AF field (mT)
NRM = 8.73 x 10-4 Am-1
PCA (10-70 mT)
dec 273.9°
inc 69.5°
MAD 2.0°
Harbour deposit (unit D)
C) Coarse sand, 449 cm
NRM = 1.06 x 10-3 Am-1
PCA (10-50 mT)
dec 204.4°
inc -44.3°
MAD 6.8°
Magnetisation (10-4 Am-1)
AF field (mT)
Hyperpycnal deposit (unit C)
D) Sand, 492 cm
NRM = 1.59 x 10-4 Am-1
PCA (10-60 mT)
dec 332.0°
inc 53.4°
MAD 3.8°
Magnetisation (10-4 Am-1)
AF field (mT)
Dredged deposit (unit B)